

A Giant Metrewave Radio Telescope survey for associated HI 21 cm absorption in the Caltech-Jodrell Flat-spectrum sample.

J. N. H. S. Aditya^{1,2*}, Nissim Kanekar^{2†}

¹*Inter-University Centre for Astronomy and Astrophysics, Pune 411007, India*

²*National Centre for Radio Astrophysics, Tata Institute of Fundamental Research, Pune 411007, India*

Accepted XXX. Received YYY; in original form ZZZ

ABSTRACT

We report a Giant Metrewave Radio Telescope (GMRT) survey for associated HI 21-cm absorption from 50 active galactic nuclei (AGNs), at $z \approx 0.04 - 3.01$, selected from the Caltech-Jodrell Bank Flat-spectrum (CJF) sample. Clean spectra were obtained towards 40 sources, yielding two new absorption detections, at $z = 0.229$ towards TXS 0003+380 and $z = 0.333$ towards TXS 1456+375, besides confirming an earlier detection, at $z = 1.277$ towards TXS 1543+480. There are 92 CJF sources, at $0.01 \lesssim z \lesssim 3.6$, with searches for associated HI 21-cm absorption, by far the largest uniformly-selected AGN sample with searches for such absorption. We find weak ($\approx 2\sigma$) evidence for a lower detection rate of HI 21-cm absorption at high redshifts, with detection rates of $28_{-8}^{+10}\%$ and $7_{-4}^{+6}\%$ in the low- z ($z < z_{\text{med}}$) and high- z ($z > z_{\text{med}}$) sub-samples, respectively. We use two-sample tests to find that the strength of the HI 21-cm absorption in the AGNs of our sample depends on both redshift and AGN luminosity, with a lower detection rate and weaker absorption at high redshifts and high ultraviolet/radio AGN luminosities. Unfortunately, the luminosity bias in our sample, with high-luminosity AGNs arising at high redshifts, implies that it is not currently possible to identify whether redshift evolution or AGN luminosity is the primary cause of the weaker absorption in high- z , high-luminosity AGNs. We find that the strength of HI 21-cm absorption does not depend on AGN colour, suggesting that dust extinction is not the main cause of reddening in the CJF sample.

Key words: galaxies: active - quasars: absorption lines - galaxies: high redshift - radio lines: galaxies

1 INTRODUCTION

Neutral hydrogen (HI) is an important constituent of the gas in the environments of active galactic nuclei (AGNs). For radio-loud AGNs, the HI 21-cm transition allows the presence of such gas to be discerned, and its kinematics studied, via HI 21-cm absorption studies against the AGN radio continuum. Such “associated” HI 21-cm absorption studies allow a detailed probe of physical conditions in AGN environments (see, e.g., Morganti & Oosterloo 2018, for a recent review), and their evolution with redshift. For example, one can test whether the strength of the HI 21-cm absorption depends on the nature of the AGN (e.g. core-dominated or lobe-dominated, high-luminosity or low-luminosity, flat spectrum or steep spectrum, etc), providing information on the distri-

bution and the excitation of neutral gas in different AGN environments. One might also test whether the strength of HI 21-cm absorption depends on redshift: weaker HI 21-cm absorption in typical AGNs over some range of redshifts might indicate a paucity of gas in the AGN environments at this epoch, shedding light on the gas accretion process and the fuelling of AGNs. The HI 21-cm absorption velocity, relative to the AGN redshift, also contains information on local conditions, with redshifted (relative to the AGN) absorption indicating the presence of inflowing gas, and blueshifted absorption, a signature of gas outflows. If the associated HI 21-cm absorption systematically arises at higher velocities than the AGN redshift, it would suggest that neutral gas is predominantly flowing towards typical AGNs at this redshift, which could fuel the nuclear activity (e.g. van Gorkom et al. 1989). Conversely, mostly blueshifted HI 21-cm absorption would imply a predominance of gas outflows, that might result in shutting down of the AGN activity (e.g. Vermeulen

* adityaj@iucaa.in

† Swarnajayanti Fellow; nkanekar@ncra.tifr.res.in

et al. 2003; Gupta et al. 2006). Similarly, narrow H I 21-cm lines with velocity spreads $\lesssim 100 \text{ km s}^{-1}$ and relatively small velocity offsets from the AGN systemic redshift are likely to indicate gas clouds with low velocity dispersion, perhaps rotating in a circumnuclear disk (e.g. Dwarakanath et al. 1995; Conway 1999; Geréb et al. 2015). Broad absorption features, with widths $\approx 200\text{--}300 \text{ km s}^{-1}$ suggest the presence of unsettled gas, possibly interacting with the active nucleus. Finally, the broadest lines, with widths $\gtrsim 500 \text{ km s}^{-1}$, are likely to arise due to interactions between the neutral gas and the radio jets in powerful radio sources (e.g. Morganti et al. 2003, 2005; Mahony et al. 2013).

A further important advantage of H I 21-cm absorption studies in probing AGN environments stems from the fact that the radio emission is often extended, stemming from both the AGN core and structures such as jets, lobes, hotspots, etc. This allows the exciting possibility of using very long baseline interferometry (VLBI) techniques to map the H I 21-cm absorption against the extended radio continuum, on scales of $\approx 10\text{--}1000 \text{ pc}$, to determine the spatial structure of the absorbing gas, and connections with the radio continuum (e.g. Mundell et al. 1995; Carilli et al. 1998a; Peck & Taylor 1998; Peck et al. 1999; Conway 1999; Beswick et al. 2002; Morganti et al. 2004; Labiano et al. 2006; Struve & Conway 2012; Morganti et al. 2013). Such VLBI absorption mapping studies are critical to identify the location of the absorbing gas in the AGN environment.

Since the first detection of associated H I 21-cm absorption, by Roberts (1970) in NGC5128, a large number of searches for associated H I 21-cm absorption have been carried out, using a variety of radio telescopes. More than 400 AGNs have so far been searched for associated H I 21-cm absorption, with more than seventy-five detections (e.g. Dickey 1986; van Gorkom et al. 1989; Carilli et al. 1998b; Moore et al. 1999; Gallimore et al. 1999; Morganti et al. 2001, 2005; Pihlström et al. 2003; Vermeulen et al. 2003; Gupta et al. 2006; Chandola et al. 2011; Allison et al. 2012; Geréb et al. 2015; Maccagni et al. 2017; Aditya & Kanekar 2018). Molecular absorption has also been detected in a handful of these systems, indicating the presence of dense gas (e.g. Gardner & Whiteoak 1976; Wiklind & Combes 1994; Wiklind & Combes 1996; Kanekar & Chengalur 2002, 2008). However, the vast majority of the detections of H I 21-cm absorption are at low redshifts, $z < 0.25$ (e.g. van Gorkom et al. 1989; Geréb et al. 2015; Maccagni et al. 2017): the current sample of associated H I 21-cm absorbers is dominated by the 59 detections of Geréb et al. (2015) and Maccagni et al. (2017), at $0.05 < z < 0.25$. Further, most searches for redshifted H I 21-cm absorption have been in highly heterogeneous samples, making it hard to differentiate between the causes for the presence or absence of absorption (e.g. redshift, AGN type, AGN luminosity, etc.). We have hence been using the Giant Metrewave Radio Telescope (GMRT) survey for redshifted associated H I 21-cm absorption towards a uniformly-selected AGN sample, distributed over a wide redshift range. Earlier results from this survey were reported in Aditya et al. (2016) and Aditya et al. (2017).

2 THE AGN TARGETS: THE CALTECH-JODRELL FLAT-SPECTRUM SAMPLE

Our primary goal was to carry out a large survey for H I 21-cm absorption from AGNs at high redshifts, $z \gtrsim 1$, to study redshift evolution in AGN environments. Of course, an important goal was to significantly increase the number of known associated H I 21-cm absorbers at high redshifts. We also aimed to target a uniformly-selected AGN sample, to minimize the heterogeneity in our AGN environments. Earlier studies at low redshifts had found evidence for a higher detection rate of H I 21-cm absorption ($\approx 40\%$) in more compact radio sources, the GHz-Peaked Spectrum (GPS) sources and the Compact Steep Spectrum (CSS) sources, than in more extended radio galaxies ($\approx 15\%$; e.g. Vermeulen et al. 2003; Gupta et al. 2006). Similarly, Pihlström et al. (2003) found that GPS sources have typically higher H I 21-cm optical depths than even the somewhat larger CSS sources. Foreground H I clouds of a given size would obscure a larger fraction of the radio emission from a compact source than from an extended source: lower observed integrated H I 21-cm optical depths towards extended radio sources can thus be naturally explained by such covering factor effects. At a fixed observed H I 21-cm optical depth sensitivity, the likelihood of detecting H I 21-cm absorption is hence higher towards compact radio sources. To maximize our chances of detections of H I 21-cm absorption, which would allow us to trace the distribution and kinematical properties of neutral gas in high- z AGN environments, we hence chose source compactness, i.e. an inverted or a flat low-frequency radio spectrum (e.g. Kellermann & Pauliny-Toth 1981; Shu 1991; O’Dea 1998), as the main criterion in sample selection.

We aimed to ensure homogeneity in our target AGNs by selecting them from a near-complete, flux-density limited sample, the Caltech-Jodrell Bank Flat-spectrum (CJF) sample (Pearson & Readhead 1988; Henstock et al. 1995; Taylor et al. 1996). The CJF sample includes all radio sources with (1) 4.85 GHz flux density $\geq 350 \text{ mJy}$, (2) flat radio spectra between 1.4 and 4.85 GHz, with $\alpha_{1.4\text{ GHz}}^{4.85\text{ GHz}} \geq -0.5$, and (3) declination $\delta > 35^\circ$ (Taylor et al. 1996), with a total of 293 sources, at redshifts $0 \lesssim z \lesssim 4.0$.

At the beginning of our survey, 29 sources of the CJF sample had been earlier searched for associated H I 21-cm absorption, mostly at $z < 1$, with a detection rate of $\approx 40\%$ (e.g. Vermeulen et al. 2003; Gupta et al. 2006). We aimed to search for associated H I 21-cm absorption from the remaining 82 CJF sources for which the redshifted H I 21-cm line frequency lies in the GMRT 327 MHz, 610 MHz and 1420 MHz observing bands (which cover the frequency ranges 300–360 MHz, 570–660 MHz, and 1000–1450 MHz, respectively). Finally, we were unable to observe 8 of the above 82 CJF sources, five at $1.1 < z < 1.5$ (CJ2 1534+501, 7C 1550+5815, CJ2 1308+471, S5 0454+84, and TXS 1851+488) and three at $3.0 < z < 3.6$ (S4 0636+68, BZQ J1526+6650, and B3 1839+389), due to their low flux densities that would have required prohibitively large integration times to achieve a good H I 21-cm optical depth sensitivity.

Our initial GMRT observations of 24 AGNs of the CJF sample were presented, and the results discussed, by Aditya et al. (2016), and an additional detection of H I 21-cm absorption at $z \approx 1.223$ towards TXS 1954+513 was presented

and discussed by Aditya et al. (2017). In the present paper, Section 3 describes the new GMRT observations, data analysis, and results for 50 AGNs of our target sample, Section 4 discusses the individual detections of HI 21-cm absorption, while Section 5 discusses the dependence of the strength of the HI 21-cm absorption on various AGN properties.

3 OBSERVATIONS, DATA ANALYSIS, AND RESULTS

3.1 The GMRT observations and data analysis

The GMRT 327 MHz, 610 MHz, and 1420 MHz receivers were used to carry out a search for associated HI 21-cm absorption from the 49 AGNs of the CJF sample without earlier searches for such absorption. We also observed the AGN TXS 1543+480, at $z = 1.277$, to confirm the detection of HI 21-cm absorption by Curran et al. (2013). The observations were carried out over 2014 April to 2015 August, in GMRT Cycles 26 (proposal 26_052, PI: Kanekar) and 28 (proposal ID: 28_089, PI: Aditya), using the GMRT Software Backend (GSB) as the correlator. 21 sources were observed with the 1420 MHz receivers, 28 with the 610 MHz receivers, and one with the 327 MHz receivers. Bandwidths of 16.7 MHz or 33.3 MHz were used for all observations, sub-divided into 512 channels, and centred at the redshifted HI 21-cm line frequency, with two circular polarizations. This yielded velocity resolutions of, respectively, $\approx 8\text{--}34\text{ km s}^{-1}$, and velocity coverages of $\approx 3600\text{--}17500\text{ km s}^{-1}$, in the different observing bands. The velocity coverage was sufficient to detect wide (velocity spread $\approx 1000\text{ km s}^{-1}$) HI 21-cm absorption, while the velocity resolution allowed excellent sensitivity to even relatively narrow ($\approx 20\text{ km s}^{-1}$) spectral components.

A standard flux density calibrator (3C48, 3C147 or 3C286) was observed at the start or end of each observing run. Observations of the target source were split into $\approx 30\text{--}40$ minute scans, bracketed by short (≈ 6 minutes) scans on a nearby phase calibrator. The flux and/or phase calibrators were also used to calibrate the system passband; no additional observations of bandpass calibrators were carried out. The on-source observing times were $\approx 1\text{--}1.5$ hours for sources observed with the 610 MHz and 1420 MHz receivers, and ≈ 3 hours for the lone source observed with the 327 MHz receivers.

Our initial GMRT observations yielded tentative detections of HI 21-cm absorption in two sources, TXS 0003+380 and TXS 1456+375, besides confirming the detection of HI 21-cm absorption in TXS 1543+480 (Curran et al. 2013). The first two sources were re-observed with the GMRT to confirm the reality of the absorption. These observations again used the GSB as the backend, but with a bandwidth of 4.17 MHz, sub-divided into 512 channels, and centred at the frequency of the putative HI 21-cm absorption feature. This provided a higher velocity resolution of $\approx 2.2\text{ km s}^{-1}$, albeit with a narrower velocity coverage $\approx 1175\text{ km s}^{-1}$. The observational details are summarized in Table 1.

All data were analysed using the Astronomical Image Processing System (AIPS; Greisen 2003) package, following standard procedures for data editing, gain and bandpass calibration, self-calibration, and imaging (see, e.g., Aditya

et al. 2016). These procedures yielded a continuum image of the field at the observing frequency and the final spectral line cube (after subtracting out all continuum emission). The HI 21-cm spectrum was extracted from the spectral cube by taking a cut along the frequency axis at the location of the target AGN. The final spectrum was then obtained by subtracting out a second-order polynomial baseline, fit to line- and RFI-free regions, to compensate for any residual bandpass effects.

3.2 Results

For ten sources, half at $z \approx 0.29\text{--}0.32$, the GMRT data were severely affected by RFI around the redshifted HI 21-cm line frequency and it was not possible to obtain reliable RFI-free spectra. In most cases, the continuum data themselves were badly affected by the RFI, rendering the flux density estimates unreliable. These sources are indicated by the label ‘‘RFI’’ in Table 1.

Except for TXS 0344+405, all the AGNs of our sample are compact in the GMRT continuum images, unresolved by the GMRT synthesized beam. The AGN flux densities at the redshifted HI 21-cm line frequency were measured by fitting a single-Gaussian model to a small region of the image plane around the target, using the AIPS task JMFIT. The measured flux densities are listed in Table 1. We note that the JMFIT measurement errors are < 1 mJy in all cases; however, the errors on the flux densities are dominated by systematic effects, $\approx 10\%$ (from our experience) for the GMRT at these frequencies. TXS 0344+405 shows extended radio structures, consisting of a central core and two extended emission components, with a typical Fanaroff-Riley II morphology (Fanaroff & Riley 1974). Since our aim is to search for neutral gas in the environments of compact AGNs, we have considered the HI 21-cm absorption spectrum against only the core of TXS 0344+405 in the later analysis.

We obtained two new detections of associated HI 21-cm absorption, at $z = 0.229$ towards TXS 0003+380 and $z = 0.333$ towards TXS 1456+375, and also confirmed the detection of HI 21-cm absorption at $z = 1.277$ towards TXS 1543+480. The HI 21-cm absorption spectra towards these AGNs are shown in Fig. 1, with flux density (in mJy) plotted against velocity (in km s^{-1}), relative to the AGN redshift. For the new detections, the HI 21-cm absorption spectra are from the confirming runs, at finer velocity resolution. The velocity-integrated HI 21-cm optical depths for these sources are $1.943 \pm 0.057\text{ km s}^{-1}$ (TXS 0003+380), $3.834 \pm 0.079\text{ km s}^{-1}$ (TXS 1456+375), and $9.56 \pm 0.36\text{ km s}^{-1}$ (TXS 1543+480). We note that our measured integrated HI 21-cm optical depth for TXS 1543+480 is in excellent agreement with the estimate of $9.69 \pm 0.53\text{ km s}^{-1}$ by Curran et al. (2013).

For 37 AGNs, the spectra were found to be consistent with noise, with no evidence for HI 21-cm absorption; these are shown in Fig. A1 in the Appendix, in order of increasing redshift. The shaded regions in the spectra indicate velocity ranges that were corrupted by RFI. The figure includes three spectra for TXS 0344+405, towards the core and the two extended radio lobes, none of which show HI 21-cm absorption.

For the non-detections, we obtained 3σ upper limits to the velocity-integrated HI 21-cm optical depth by assuming

Table 1. The 50 target sources, in order of increasing redshift.

Source	z	$\nu_{21\text{-cm}}$ MHz	S_ν^b mJy	$\Delta\nu$ km s ⁻¹	Beam "×"	ΔS mJy	$\int \tau dv^c$ km s ⁻¹	N_{HI}^d ×10 ²⁰ cm ⁻²
TXS 0344+405 ^C	0.039	1367.08	24.3	28.6	7.0 × 6.4	1.7	< 14	< 26
TXS 0344+405 ^{SE}	0.039	1367.08	82.4	28.6	7.0 × 6.4	1.8	< 4.9	< 8.9
TXS 0344+405 ^{NW}	0.039	1367.08	89.1	28.6	7.0 × 6.4	2.0	< 5.5	< 10
TXS 0733+597	0.041	1364.46	502.8	28.6	3.9 × 2.7	1.5	< 0.67	< 1.2
S5 2116+81	0.084	1310.33	137.2	14.9	7.4 × 3.6	1.2	< 1.4	< 2.5
TXS 1418+546	0.153	1231.92	595.6	31.7	4.1 × 2.9	2.4	< 1.5	< 2.7
S4 0749+54	0.200	1183.67	533.3	32.9	3.6 × 2.9	2.7	< 1.8	< 2.1
TXS 0003+380	0.229	1155.74	547.3	2.1 ^a	4.5 × 3.5	2.6	1.943 ± 0.057	3.54 ± 0.11
S5 1356+47	0.230	1154.80	544.8 ^e	16.9	RFI	–	–	–
TXS 0010+405	0.255	1131.79	358.9	34.5	3.1 × 2.5	2.3	< 1.4	< 2.5
TXS 1719+357	0.263	1124.63	262.4	34.7	4.5 × 3.4	1.4	< 1.2	< 2.2
B3 0251+393	0.289	1101.94	229.8 ^e	8.9	RFI	–	–	–
TXS 0716+714	0.300	1092.62	834.8 ^e	17.9	RFI	–	–	–
TXS 1700+685	0.301	1091.78	372.9 ^e	8.9	RFI	–	–	–
S5 1928+73	0.302	1090.94	4058.9 ^e	17.9	RFI	–	–	–
JVAS J1010+8250	0.322	1074.40	532.1 ^e	18.2	RFI	–	–	–
TXS 0424+670	0.324	1072.81	719.1	36.4	8.6 × 4.1	2.9	< 0.89	< 1.6
B3 1456+375	0.333	1065.57	148.4	2.3 ^a	9.1 × 3.8	1.6	3.834 ± 0.079	6.98 ± 0.15
S5 2007+77	0.342	1058.42	660.0	36.9	4.8 × 4.0	24.3	< 9.9	< 18
TXS 0035+367	0.366	1039.82	581.2	37.5	5.6 × 4.9	1.2	< 0.51	< 0.93
TXS 0954+658	0.368	1038.30	1104.8	37.6	5.6 × 4.2	20.1	< 5.8	< 11
CJ2 0925+504	0.370	1036.79	310.4	37.7	4.1 × 3.6	1.6	< 1.2	< 2.2
TXS 0110+495	0.389	1022.61	615.4	38.2	4.8 × 4.0	1.6	< 0.43	< 0.78
TXS 1030+415	1.117	670.95	636.6	29.1	7.2 × 4.0	2.2	< 0.69	< 1.3
TXS 0249+383	1.122	669.37	877.0 ^e	29.2	RFI	–	–	–
S5 1044+71	1.150	660.65	1522.9	29.5	10.6 × 3.9	2.9	< 0.38	< 0.69
8C 1305+804	1.183	650.67	1334.2 ^e	30.1	RFI	–	–	–
TXS 1105+437	1.226	638.09	406.5	30.6	10.5 × 6.5	1.3	< 0.70	< 1.3
TXS 1015+359	1.228	637.52	702.7	30.5	8.3 × 4.8	1.3	< 0.43	< 0.78
TXS 1432+422	1.240	634.10	286.1	30.8	5.9 × 5.4	1.2	< 0.95	< 1.7
S5 1150+81	1.250	631.29	1788.1	30.9 ^d	15.7 × 6.1	8.8	< 1.1	< 2.0
TXS 1020+400	1.254	630.17	1496.5	30.9	13.2 × 6.8	3.6	< 0.51	< 0.93
S5 1039+81	1.260	628.49	726.5	31.1 ^a	16.1 × 5.8	5.2	< 1.5	< 2.8
TXS 1543+480 ^f	1.277	623.81	861.5	31.3 ^d	8.0 × 5.3	2.1	9.56 ± 0.36	17.43 ± 0.66
TXS 1656+571	1.281	622.71	1456.3	31.3	23.4 × 12.6	4.9	< 0.74	< 1.4
TXS 0833+416	1.301	617.29	432.2	31.6 ^d	7.5 × 4.7	1.8	< 0.63	< 1.1
TXS 2138+389	1.306	615.96	612.5 ^e	15.9	RFI	–	–	–
TXS 2319+444	1.310	614.89	378.4	31.7	9.2 × 5.3	1.3	< 0.65	< 1.9
TXS 1240+381	1.318	612.77	547.2	31.8	6.6 × 4.6	1.6	< 0.63	< 1.1
TXS 2007+659	1.325	610.92	631.1	31.9	10.4 × 4.6	2.3	< 0.76	< 1.4
JVAS J2236+7322	1.345	605.71	270.7	32.2	13.9 × 6.4	1.3	< 0.97	< 1.8
TXS 1342+663	1.351	604.17	231.8	32.3	11.1 × 6.3	1.1	< 0.98	< 1.8
TXS 1739+522	1.375	598.06	1006.7	32.6	8.9 × 4.9	2.9	< 0.58	< 1.1
TXS 1442+637	1.380	596.80	656.6	32.7 ^d	9.2 × 4.3	5.4	< 1.3	< 2.3
TXS 1010+350	1.410	589.37	520.1	33.1	9.5 × 6.6	1.8	< 0.67	< 1.2
TXS 2229+695	1.413	588.64	291.4	33.1	10.3 × 3.5	2.7	< 1.7	< 3.1
TXS 0145+386	1.442	581.65	207.4	33.6	9.3 × 6.5	1.3	< 1.2	< 2.2
JVAS J2311+4543	1.447	580.46	156.4	33.6	13.6 × 5.7	1.7	< 2.2	< 3.9
S5 1058+72	1.460	577.40	1499.7	33.8	14.0 × 4.6	2.3	< 0.31	< 0.57
B3 1746+470	1.484	571.82	187.9	34.1	9.9 × 8.5	4.2	< 4.5	< 8.2
TXS 0859+681	1.499	568.39	458.4 ^e	34.3	RFI	–	–	–
TXS 1427+543	3.013	353.95	2402.7	27.6	16.6 × 8.0	7.4	< 0.44	< 0.81

^a This spectrum has not been Hanning-smoothed and resampled.^b Flux densities are measured using the task JMFIT.^c The upper limits on the integrated HI optical depth assuming a line FWHM of 100 km s⁻¹.^d The HI column density is calculated for an assumed spin temperature of 100 K.^e The flux density of the source at the redshifted HI line frequency was estimated by interpolating between the 1.4 GHz flux density (from the FIRST or NVSS surveys; Becker et al. 1995; Condon et al. 1998) and the 325 or 365 MHz flux density (from the WENSS and Texas surveys, respectively; Rengelink et al. 1997; Douglas et al. 1996) in the literature.^f The detection of associated HI 21-cm absorption towards this source was originally reported by Curran et al. (2013).

For TXS 0344+405, "C" corresponds to the core, "SE" to the south-east lobe, and NW to the north-west lobe.

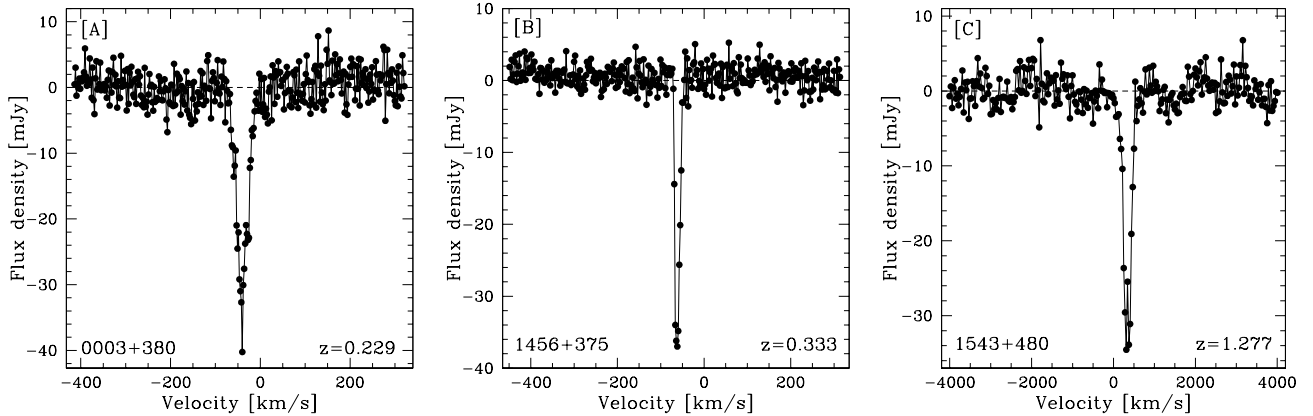


Figure 1. The GMRT HI 21-cm absorption spectra towards [A] TXS 0003+380 at $z = 0.229$, [B] TXS 1456+375 at $z = 0.333$, and [C] TXS 1543+480, at $z = 1.277$. In all panels, the bottom axis contains velocity, in km s^{-1} , relative to the AGN redshift (listed in each panel).

a line full-width-at-half-maximum (FWHM) of 100 km s^{-1} , and measuring the root-mean-square (RMS) optical depth noise from RFI-free channels after smoothing each spectrum to approximately the same resolution. For two sources, TXS 0954+658 and S5 2007+77, a weak ripple was found to be present across the observing band, probably due to time variability in the antenna bandpass shapes that could not be calibrated out. Attempts to excise these ripples by data editing were unsuccessful. Since the peak-to-peak amplitude of the ripple is relatively low, the spectra may still be used to constrain the presence of strong HI 21-cm absorption. Hence, for these two sources, we conservatively estimated the upper limit to the HI 21-cm optical depth to be $3 \times$ the peak-to-peak spread in the ripple in the optical depth spectrum.

Table 1 summarizes the observational details and results from our GMRT observations, with the sources ordered by increasing redshift. The columns of the table are (1) the AGN name, (2) the AGN redshift, z (3) the redshifted HI 21-cm line frequency, $\nu_{21\text{cm}}$, in MHz, (4) the AGN flux density, S_ν , at the redshifted HI 21-cm line frequency, in mJy, (5) the velocity resolution ΔV of the final HI 21-cm spectrum, in km s^{-1} , (6) the FWHM of the synthesized beam, in “x”, (7) the RMS noise ΔS on the final spectrum at the velocity resolution of column (5), in mJy, (7) the integrated HI 21-cm optical depth $\int \tau d\nu$ in km s^{-1} , or, for non-detections, the 3σ upper limit to $\int \tau d\nu$, assuming a line FWHM of 100 km s^{-1} , (8) the HI column density N_{HI} in cm^{-2} , or, for non-detections, the 3σ upper limit to N_{HI} , assuming a spin temperature (T_s) of 100 K. For the ten sources affected by RFI, the sixth column contains “RFI”, and the remaining columns indicate that no information is available. In most cases, the velocity resolution quoted in column (5) is after Hanning-smoothing and resampling the spectrum.

4 THE DETECTIONS OF HI 21-cm ABSORPTION

In this section, we discuss the detections of HI 21-cm absorption and the implications of our results for conditions in the AGN environment.

4.1 The $z = 0.229$ absorber towards TXS 0003+380

The radio emission of TXS 0003+380 is unresolved in the GMRT continuum image at $\approx 1156 \text{ MHz}$, with no evidence of any extended structure. A prominent core is present in the milli-arcsec (mas) scale VLBI map at 2.3 GHz, along with a weak signature of a jet projected towards the south-west (Fey & Charlot 2000). More than 95% of the 2.3 GHz flux density arises from the core, with a total of only $\approx 35 \text{ mJy}$ arising from the components in the radio jet (see Table 2 of Fey & Charlot 2000). The AGN spectrum is very flat at low radio frequencies, $\lesssim 5 \text{ GHz}$, with flux densities of $\approx 500 - 800 \text{ mJy}$ over the wide frequency range 74 – 5000 MHz. The radio flux density is known to vary rapidly, on a timescale of 2 – 20 days (Heeschen 1984). Such ‘flickering’ may arise due to new plasma ejections, when the radiation is highly beamed towards the observer (Ghisellini et al. 1993). Optical and X-ray studies of this source also find evidence for strong blazar characteristics (e.g. Massaro et al. 2009).

The GMRT HI 21-cm absorption spectrum towards TXS 0003+380 is shown in Fig. 1[A]. The absorption has a peak line depth of $\approx 40 \text{ mJy}$, comparable to the total flux density ($\approx 35 \text{ mJy}$) in the jet components at 2.3 GHz. This indicates that the absorption is likely to arise against the radio core. The absorption line is relatively narrow, with a full width between 20% points of only $\approx 45 \text{ km s}^{-1}$. The detected HI 21-cm absorption implies an HI column density of $(3.54 \pm 0.11) \times (T_s/100 \text{ K}) \times 10^{20} \text{ cm}^{-2}$. While the HI 21-cm absorption appears to be blueshifted by $\approx 50 \text{ km s}^{-1}$ from the AGN redshift ($z = 0.229$; Stickel & Kühr 1994), we note that the latter authors do not quote an error on their redshift estimate.

4.2 The $z = 0.333$ absorber towards TXS 1456+375

TXS 1456+375 is unresolved in the GMRT 1065 MHz continuum image, and is also extremely compact in the VLBI 5 GHz image of Helmboldt et al. (2007), with a linear size $\lesssim 10 \text{ mas}$. The AGN spectrum is flat at low frequencies, with spectral index $\alpha = -0.02$ between 408 MHz and 1.4 GHz, steepening slightly to $\alpha = -0.27$ between 1.4 GHz and 5 GHz (Helmboldt et al. 2007). The source has been classified as a blazar in the literature, based on its optical and near-

infrared properties (e.g. Massaro et al. 2009; Davenport et al. 2015). Our line of sight is hence likely to lie close to the direction of any jet emission. In addition, the AGN spectrum rises steeply with increasing wavelength in the optical and near-infrared bands, with $R-K=5.14$ mag, causing it to be classified as a “red” quasar (Glikman et al. 2012).

The GMRT H I 21-cm absorption spectrum towards TXS 1456+375 is displayed in Fig. 1[B]. The H I 21-cm absorption is only marginally offset from the AGN redshift ($z = 0.33343 \pm 0.00017$; Schneider et al. 2005), with the deepest absorption blueshifted by $\approx 60 \text{ km s}^{-1}$ (consistent with the AGN redshift within $\approx 2\sigma$ significance). The H I 21-cm absorption is very narrow, with a width between 20% points of only $\approx 20 \text{ km s}^{-1}$, and no evidence of extended absorption. The H I column density inferred from the H I 21-cm absorption is $(6.98 \pm 0.15) \times (T_s/100 \text{ K}) \times 10^{20} \text{ cm}^{-2}$. The small angular extent of the 5 GHz radio emission implies that the detected H I 21-cm absorption probably arises against the radio core.

4.3 The $z = 1.277$ absorber towards TXS 1543+480

TXS 1543+480 is unresolved in our GMRT 624 MHz continuum image, but shows two clear lobes, with similar flux densities, in the 5 GHz VLBI image (Helmboldt et al. 2007). The authors classify this source as a candidate Compact Symmetric Object (CSO). CSOs have symmetric parsec-scale structure, dominated by steep-spectrum extended emission on both sides of the core. The core is usually faint, or even undetected, in such sources. It is plausible that the two radio components detected in the 5 GHz VLBI image of TXS 1543+480 arise from parsec-scale lobes at the ends of VLBI-scale jets, with the core remaining undetected. Multi-frequency VLBI studies are needed to measure the spectral indices of the mas-scale radio components, and to test whether both have steep spectra, as expected for a CSO. At present, only 5 GHz VLBI images are available for TXS 1543+480 in the literature and it hence remains a candidate CSO (Helmboldt et al. 2007).

If TXS 1543+480 is indeed a CSO, its 624 MHz flux density is likely to be dominated by the emission from the two radio lobes, as these would be expected to have steep spectra. The detected H I 21-cm absorption is hence likely to arise against one or both of the VLBI radio lobes. The H I 21-cm absorption is quite extended, with a width between 20% points of $\approx 330 \text{ km s}^{-1}$. Such wide absorption could arise either due to absorption against both radio lobes, or due to disturbed gas that is interacting with the AGN jets.

We have earlier reported a similar case of associated H I 21-cm absorption towards another CSO, TXS 1245-197 at $z = 1.275$ (Aditya & Kanekar 2018). It is intriguing that both TXS 1543+480 and TXS 1245-197 show wide H I 21-cm absorption, with widths of $\gtrsim 300 \text{ km s}^{-1}$ between 20% points. Earlier studies of the kinematic ages of CSOs have been used to argue that CSOs are small due to their youth, and not because they are “frustrated” sources that reside in a dense environment, unable to grow to large sizes (Owsianik & Conway 1998; Owsianik et al. 1998; Taylor et al. 2000). However, our detections of wide H I 21-cm absorption from CSO environments support the notion that the radio jets in CSOs may indeed be evolving in a dense gaseous environment, with their expansion constrained by the surrounding medium.

5 DISCUSSION

5.1 A uniformly-selected flat-spectrum sample

Searches for redshifted associated H I 21-cm absorption have so far been carried out in more than 400 AGNs, with $\gtrsim 75$ detections of H I 21-cm absorption (e.g. van Gorkom et al. 1989; Vermeulen et al. 2003; Gupta et al. 2006; Curran et al. 2010; Geréb et al. 2015; Maccagni et al. 2017). The vast majority of both searches and detections are at low redshifts, $z < 1$, where the typical detection fraction is $\approx 30\%$ (e.g. Pihlström et al. 2003; Gupta et al. 2006; Maccagni et al. 2017). The situation is very different at high redshifts, $z > 1$, with searches for associated H I 21-cm absorption in only ≈ 25 AGNs (e.g. Gupta et al. 2006; Curran et al. 2013) and just four detections in the literature, prior to our survey. The implied detection rate of H I 21-cm absorption is $\approx 16^{+13}_{-8}\%$, where the errors are from Poisson statistics (Gehrels 1986). While the detection rate of H I 21-cm absorption at $z > 1$ is only half that at low redshifts, the difference between the two is not statistically significant due to the large uncertainty in the high- z value, simply due to the fact that few high- z AGNs have hitherto been targeted in H I 21-cm absorption studies. An important part of the present survey was simply to increase the number of searches for redshifted H I 21-cm absorption at $z > 1$. If high- z AGNs yield a detection fraction similar to those at low redshifts, the survey would then yield a large sample of associated H I 21-cm absorbers, suitable for detailed kinematic studies of AGN environments. Conversely, if the detection fraction remains low at $z > 1$, this would be evidence for redshift evolution in AGN environments.

Further, most studies of associated H I 21-cm absorption (e.g. Vermeulen et al. 2003; Gupta et al. 2006; Curran et al. 2013; Maccagni et al. 2017) have targeted highly heterogeneous AGN samples at all redshifts. This heterogeneity makes it difficult to distinguish between possible redshift evolution in the AGN environment and differences in the AGN samples at different redshifts. For example, Gupta et al. (2006) carried out an analysis of 96 AGNs, mostly at low to intermediate redshifts, $z < 1$. They found little evidence for redshift evolution in either the detection rates of H I 21-cm absorption or in the distribution of the H I 21-cm optical depths. However, their sample included a range of AGN types, with 21 large radio galaxies, 13 flat-spectrum sources, 35 CSS sources, and 27 GPS sources. The heterogeneity of the sample makes it difficult to reliably interpret the observational data.

An alternative explanation for the tentative result that the strength of associated H I 21-cm absorption may be weaker at high redshifts stems from the luminosity bias in most AGN samples used in such studies. High- z AGN samples typically contain more objects with higher rest-frame UV and radio luminosities. Curran et al. (2008) suggest that the high AGN luminosity in the UV and/or radio wavebands could lead to a lower H I 21-cm optical depth, either by ionizing the H I (and thus reducing the H I column density) or by altering the hyperfine level populations (and thus increasing the spin temperature). Curran et al. (2008) hence argued that the high luminosities of high- z AGNs may be the primary cause of the low detection rate of associated H I 21-cm absorption at high redshifts (see also Curran et al. 2013). However, we note that the AGN samples of Curran et al.

(2008) and Curran et al. (2013) were also highly heterogeneous, containing all the AGNs that had been searched for HI 21-cm absorption in the literature.

The present survey for HI 21-cm absorption aims to address the above issues by carrying out a search for HI 21-cm absorption in a large and uniformly-selected sample of AGNs, selected from the CJF catalogue, to investigate the dependence of the HI 21-cm absorption strength and detectability on redshift and AGN properties (e.g. luminosity, colour, spectral index, etc). In our pilot study (Aditya et al. 2016), we combined 23 new searches for redshifted HI 21-cm absorption with 29 searches from the literature (all in AGNs from the CJF sample), to find tentative evidence (at $\approx 3\sigma$ significance) that the strength of associated HI 21-cm absorption depends on both redshift and AGN luminosity, with weaker HI 21-cm absorption obtained at both high redshifts and higher AGN luminosities.

In the present work, we have completed our GMRT HI 21-cm absorption survey of AGNs of the CJF sample, targeting nearly all CJF sources whose redshifted HI 21-cm line frequencies lie within the GMRT’s legacy 327, 610, and 1420-MHz bands. Including 39 sources with usable data from this study, our full sample consists of 92 flat-spectrum AGNs, which includes 63 sources from our GMRT observations and 29 from the literature. The sample contains 16 detections of HI 21-cm absorption [including the three confirmed detections of this paper towards TXS 0003+380, TXS 1456+375, and TXS 1543+480, the confirmed detection towards TXS 1954+513 (Aditya et al. 2017), and our tentative detection towards TXS 0604+728 (Aditya et al. 2016)], and 76 non-detections, yielding upper limits to the HI 21-cm optical depth. This is by far the largest sample of uniformly-selected AGNs that have been searched for associated HI 21-cm absorption. The sample covers a large redshift range, $0.01 \lesssim z \lesssim 3.6$, with more than half of the sample (≈ 50 sources) at $z > 1$.

The 92 CJF sources of our full sample are listed in order of increasing redshift, in Table 2. The columns of this table are (1) the AGN name, (2) the AGN redshift, (3) the velocity-integrated HI 21-cm optical depth in km s^{-1} , or, for non-detections of HI 21-cm absorption, the 3σ upper limit to the HI 21-cm optical depth, assuming a Gaussian profile with a line FWHM of 100 km s^{-1} , (4) the rest-frame 1216 Å AGN luminosity $L'_{UV} \equiv \text{Log}[L_{UV}/(\text{W Hz}^{-1})]$, inferred by interpolating between measured luminosities in UV and/or optical wavebands (see below), (5) the rest-frame 1.4 GHz AGN luminosity $L'_{1.4 \text{ GHz}} \equiv \text{Log}[L_{1.4 \text{ GHz}}/(\text{W Hz}^{-1})]$, (6) the AGN spectral index close to the redshifted HI 21-cm line frequency, $\alpha_{21\text{-cm}}$, (7) the AGN colour (R–K) between the R- and K-bands, (8) the reference for the search for HI 21-cm absorption, and (9) references for the estimates of UV, optical, and near-infrared (NIR) luminosities, which were used to infer L'_{UV} and (R–K).

The rest-frame 1216 Å AGN luminosity was estimated following the procedure of Curran et al. (2010). We first determined the flux density F_{UV} at $1216 \times (1+z)$ Å for each AGN, using a power-law spectrum to interpolate between measured flux densities at two nearby optical and/or UV wavebands from the literature. The luminosity at rest-frame 1216 Å was then inferred from the expression $L_{UV} = 4\pi D_{\text{AGN}}^2 F_{UV}/(1+z)$, where D_{AGN} is the AGN’s luminosity distance. For two AGNs, TXS 0424+670 and TXS 1020+400,

the flux density is known only at a single optical waveband, quite distant from the redshifted 1216 Å wavelength. These systems hence do not have a listed rest-frame 1216 Å luminosity in Table 2.

The radio spectral indices of the AGNs were computed from their flux densities at the redshifted HI 21-cm line frequency and a nearby frequency at which a flux density estimate was available in the literature. For all sources at $z > 1$, the second frequency was 1.4 GHz, from the FIRST or NVSS surveys (Becker et al. 1995; Condon et al. 1998). For sources at $z < 1$, the second frequency was either 365 MHz (the Texas survey; Douglas et al. 1996) or 325 MHz (the WENSS survey; Rengelink et al. 1997). Finally, the (R–K) colour could only be inferred for 58 AGNs of the full sample; the remaining sources do not have K-band information in the literature.

In the following sections, we will examine the dependence of the HI 21-cm detection fraction and the distribution of integrated HI 21-cm optical depth on redshift, radio spectral index, AGN radio and UV luminosities, and the (R–K) colour, for the full sample of 92 flat-spectrum sources.

5.2 Redshift evolution

Figure 2 plots the velocity-integrated HI 21-cm optical depth, in logarithmic units, against AGN redshift, for the full sample of 92 sources. It is clear that our GMRT observations, especially at $1.1 \lesssim z \lesssim 1.5$, are sufficiently sensitive to detect HI 21-cm opacities lower than those of most of the detections of HI 21-cm absorption. Further, most HI 21-cm detections are concentrated at low redshifts, $z < 1$, with 13 detections at $z < 1$, and just 3 detections at $z > 1$ (including the tentative detection at $z \approx 3.530$ towards TXS 0604+728; Aditya et al. 2016). The median redshift of the sample is $z_{\text{med}} = 1.200$. Dividing the sample at this redshift into low- z and high- z sub-samples, the former has 13 detections and 33 non-detections of HI 21-cm absorption, whereas the latter has 3 detections (one of which is tentative) and 43 non-detections. The detection rates of HI 21-cm absorption (see Fig. 3) are $28^{+10}_{-8}\%$ and $7^{+6}_{-4}\%$ (again estimating the 1σ errors from Poisson statistics; Gehrels 1986) for the $z < z_{\text{med}}$ and $z > z_{\text{med}}$ sub-samples, respectively; the high- z detection rate is even lower, $4^{+6}_{-3}\%$, when the tentative detection towards TXS 0604+728 is excluded from the sample. The high- z sub-sample thus has a lower HI 21-cm detection rate, albeit only at $\approx 2.1\sigma$ significance.

In addition to the HI 21-cm detection rates, we tested whether the distribution of the strength of the HI 21-cm absorption in AGN environments varies with redshift. For this purpose, we used survival analysis, in the ASURV package (Isobe et al. 1986), to correctly include the upper limits on the HI 21-cm opacity. Within ASURV, the Peto-Prentice generalized Wilcoxon test finds that the null result that the velocity-integrated HI 21-cm optical depths of the low- z and high- z AGN sub-samples (again separated at z_{med}) are drawn from the same distribution is ruled out at 3σ significance (increasing to 3.4σ significance when the tentative detection towards TXS 0604+728 is excluded from the sample). We thus find statistically significant evidence for redshift evolution in the strength of associated HI 21-cm absorption in a uniformly-selected AGN sample, with lower-redshift AGNs showing both a higher detection rate of HI 21-cm absorption and significantly higher integrated HI 21-cm optical depths.

Table 2. The 92 CJF sources of the full sample with searches for redshifted H_I 21-cm absorption, listed in order of increasing redshift. 63 sources are from the present survey, 39 from this paper and 24 from Aditya et al. (2016, 2017), while 29 are from the literature. See main text for discussion.

AGN	z	$\int \tau dv$ km s ⁻¹	L'_{UV} ^a	$L'_{1.4\text{ GHz}}$	$\alpha_{21\text{-cm}}$	(R-K) ^b	Refs. ^c (21-cm)	Refs. ^d (UV,Opt.,NIR)
TXS 1146+596	0.011	5.3 ± 1.8	20.30	23.09	0.26	2.3	3	1–4
TXS 0316+413	0.018	1.3	20.61	25.13	1.05	-0.2	4	1,3,4
B3 0651+410	0.022	< 0.82	18.69	23.35	0.60	-1.0	5	1,3,4
TXS 1101+384	0.030	< 0.63	21.28	24.18	0.17	-1.7	6	4,5
TXS 1744+557	0.030	< 1.2	19.53	24.02	0.22	-3.1	7	1,3,4
TXS 1652+398	0.034	< 2.4	21.58	24.56	-0.12	-1.3	6	1,3,4
TXS 0344+405	0.039	< 6.3	21.34	23.23	1.70	0.6	1	1,3,4
TXS 0733+597	0.041	< 0.67	19.69	24.24	-0.28	-1.8	1	1,3,4
TXS 1254+571	0.042	33.9 ± 3.8	20.51	24.06	-0.57	6.1	14	2–4
TXS 1807+698	0.051	<1.6	20.91	25.00	1.05	0.2	6	1,3,4
TXS 0402+379	0.055	0.98 ± 0.11	19.88	25.31	-0.29	3.6	9	3,6
TXS 1144+352	0.063	< 1.1	20.26	24.75	0.54	-0.9	7	1,3,4
TXS 2200+420	0.069	< 0.95	20.30	25.78	-0.14	2.0	6	7–10
S5 2116+81	0.084	< 1.4	21.25	24.31	-0.67	1.5	1	1,3,4
TXS 1418+546	0.153	< 1.5	21.71	25.48	0.58	4.7	1	1,4,11
TXS 1946+708	0.101	15.8 ± 4.6	18.60	25.35	-0.33	1.3	10	3,4
TXS 0309+411	0.134	< 0.92	18.48	25.23	0.08	1.5	7	3,4
S4 0749+54	0.200	< 1.2	20.71	25.68	0.35	2.5	1	1,4,11
IVS B1622+665	0.201	< 1.7	20.00	25.24	0.53	2.9	5	3,4
S5 1826+79	0.224	< 15	21.28	25.57	0.59	2.1	11	1,3,4
TXS 2021+614	0.227	< 0.21	–	26.43	0.07	3.3	11	3,4
TXS 0003+380	0.229	1.943 ± 0.057	20.62	25.80	0.49	3.6	1	1,3,4
TXS 2352+495	0.238	1.7	20.84	26.46	-0.09	2.9	11	3,4,12
TXS 0831+557	0.241	0.58	21.39	27.03	-0.15	0.3	11	1,3,4
TXS 0010+405	0.255	< 1.4	21.24	25.72	1.37	2.2	1	1,3,4
TXS 1719+357	0.263	< 1.2	21.90	25.61	0.74	3.2	1	1,3,4
TXS 1943+546	0.263	2.9	20.85	26.46	-0.45	1.4	11	1,3,6
TXS 0424+670	0.324	< 0.89	–	26.24	-0.46	–	1	–
B3 1456+375	0.333	3.834 ± 0.079	20.65	25.58	-0.41	5.1	1	1,3,7
S5 2007+77	0.342	< 9.9	22.03	26.25	0.09	3.5	1	3,7
TXS 0035+367	0.366	< 0.51	21.56	26.26	-0.17	2.4	1	1,3,4
TXS 0954+658	0.368	< 5.8	21.96	26.55	0.01	3.3	1	1,3,4
CJ2 0925+504	0.370	< 1.2	22.75	26.00	0.38	2.3	1	1,3,7
TXS 0110+495	0.389	< 0.43	21.09	26.34	-0.01	2.4	1	1,3,4
TXS 1031+567	0.459	< 0.76	19.90	26.96	-0.20	–	11	2,13
TXS 1355+441	0.646	19	20.60	26.94	-0.34	–	11	1,2,13
S4 0108+38	0.669	46 ± 7	21.63	26.95	1.16	–	12	1,14,15
TXS 1504+377	0.672	27.20 ± 0.04	20.30	26.95	-0.21	–	15	2
TXS 0923+392	0.695	< 0.54	23.47	27.49	-0.38	1.7	11	1,4,15
TS5 0950+74	0.695	< 1.4	21.65	27.15	0.92	–	11	3
TXS 1642+690	0.751	< 0.69	22.66	27.34	0.03	–	11	3
S4 1843+35	0.764	< 6.0	24.66	27.55	-0.03	–	11	3
TXS 1030+415	1.117	< 0.69	23.32	27.30	-0.61	–	1	2
TXS 0600+442	1.136	< 0.71	–	27.61	-0.37	–	2	–
S5 1044+71	1.150	< 0.38	23.26	27.70	-0.97	4.7	1	1,3,4
TXS 2356+390	1.198	< 0.42	22.36	27.36	-1.16	–	2	1,3
TXS 0821+394	1.216	< 0.44	23.55	27.97	-0.75	3.0	2	1–4
TXS 1954+513	1.223	0.698 ± 0.036	23.23	27.75	0.06	2.4	16	3,4
TXS 1105+437	1.226	< 0.70	23.04	27.18	-0.38	–	1	1,2
TXS 1015+359	1.228	< 0.43	24.31	27.42	-0.02	–	1	1
TXS 1432+422	1.240	< 0.95	22.62	27.04	0.10	–	1	1,3,4
TXS 0945+408	1.249	< 0.30	23.93	27.89	-0.46	2.5	2	1,3,4
S5 1150+81	1.250	< 1.1	23.54	27.84	-0.33	3.3	1	1,3,4
TXS 1020+400	1.254	< 0.51	–	27.77	-0.78	3.1	1	3,4
S5 1039+81	1.260	< 1.5	23.90	27.46	0.01	2.9	1	3,4

Table 2. (contd.)

AGN	z	$\int \tau dv$ km s ⁻¹	L'_{UV} ^a	$L'_{1.4\text{ GHz}}$	$\alpha_{21\text{-cm}}$	(R-K) ^b	Refs. ^c (21-cm)	Refs. ^d (UV,Opt.,NIR)
TXS 0641+392	1.266	< 0.68	22.64	27.22	0.79	–	2	3
TXS 0537+531	1.275	< 0.32	22.84	27.46	0.01	2.7	2	1,3,4
TXS 1543+480	1.277	9.69 ± 0.53	22.08	27.36	-0.23	6.3	13	1,2,4
TXS 1656+571	1.281	< 0.74	23.56	27.77	-0.54	–	1	1,3
TXS 0707+476	1.292	< 0.30	23.86	27.63	-0.15	1.4	2	1,3,4
TXS 0833+416	1.301	< 0.63	24.06	27.26	-0.02	0.2	1	1,3,4
TXS 2319+444	1.310	< 0.65	22.41	27.20	-0.05	–	1	1,3
TXS 0248+430	1.311	< 1.4	23.10	27.84	0.22	-0.9	3	1,3,4,16
TXS 1240+381	1.318	< 0.63	23.53	27.37	0.01	2.9	1	1,3,4
TXS 0850+581	1.318	< 0.37	23.53	27.63	-0.26	–	2	1
TXS 2007+659	1.325	< 0.76	22.51	27.44	-0.26	–	1	1,3
S5 2353+81	1.344	< 0.87	22.30	27.41	-0.53	2.9	2	1,3,6
JVAS J2236+7322	1.345	< 0.97	22.64	27.08	-0.01	–	1	1,3
TXS 1342+663	1.351	< 0.98	22.74	27.02	1.23	4.3	1	1–4
TXS 0035+413	1.353	< 0.76	23.12	27.39	0.35	–	2	1
TXS 1739+522	1.375	< 0.58	23.73	27.67	0.51	3.1	1	1,3,4
TXS 1442+637	1.380	< 1.3	23.90	27.51	0.05	2.0	1	1,3,4
TXS 1030+611	1.401	< 0.87	23.56	27.53	-0.37	5.3	2	1–4
TXS 1010+350	1.410	< 0.67	23.94	27.41	-0.43	–	1	1
TXS 2229+695	1.413	< 1.7	24.47	27.15	0.64	–	1	3,13
TXS 0820+560	1.418	< 0.34	23.69	27.87	-0.26	–	2	1
TXS 0805+410	1.418	< 0.69	23.32	27.40	-0.07	–	2	1,2
TXS 0804+499	1.436	< 0.95	23.45	27.54	0.31	–	2	1,2
TXS 0145+386	1.442	< 1.2	23.54	27.02	0.58	1.7	1	1,3,4
TXS 0917+624	1.446	< 0.79	23.22	27.70	0.23	3.2	2	1–4
JVAS J2311+4543	1.447	< 2.2	22.82	26.90	0.76	–	1	1,3
S5 1058+72	1.460	< 0.31	24.27	27.89	-0.21	1.9	1	1,3,4
TXS 0859+470	1.470	< 0.43	23.54	28.17	-0.23	–	2	2
TXS 2253+417	1.476	< 0.71	–	27.82	0.30	–	2	–
B3 1746+470	1.484	< 4.5	23.43	27.00	0.54	–	1	1,3
TXS 0340+362	1.484	< 3.0	22.75	27.19	0.35	–	2	3
TXS 1427+543	3.013	< 0.44	23.77	28.66	-0.60	–	1	2
TXS 0800+618	3.033	< 1.2	23.67	28.22	-0.05	–	2	1,3
TXS 0642+449	3.396	< 2.9	24.47	27.86	0.72	2.9	2	3,4,17
TXS 0620+389	3.469	< 0.20	24.28	28.50	-0.16	2.4	2	3,14,18
TXS 0604+728	3.530	4.29 ± 0.28	23.96	28.64	-0.38	–	2	1,3
TXS 0749+426	3.589	< 0.76	24.60	28.14	0.16	2.4	2	2,3,18

Notes to the table:

^aThe inferred rest-frame 1216 Å AGN luminosity, obtained by extrapolating from measurements in two nearby optical and/or ultraviolet bands. For two AGNs (indicated by a “–” in this column), the UV luminosity could not be obtained as the AGN flux density is only available at a single optical waveband in the literature.

^bFor sources with “–” entries, the flux density is not known in the K-band; the (R–K) colour hence could not be obtained.

^cReferences for the associated HI 21-cm absorption searches : (1) This paper; (2) Aditya et al. (2016); (3) Gupta et al. (2006); (4) De Young et al. (1973); (5) Orienti et al. (2006); (6) van Gorkom et al. (1989); (7) Chandola et al. (2013); (8) Dickey & Benson (1982); (9) Morganti et al. (2009); (10) Peck et al. (1999); (11) Vermeulen et al. (2003); (12) Carilli et al. (1998b); (13) Curran et al. (2013); (14) Gallimore et al. (1999); (15) Kanekar & Chengalur (2008); (16) Aditya et al. (2017).

^dReferences for the ultraviolet, optical, and infrared luminosity measurements, which were used to obtain the rest-frame 1216 Å UV luminosity (following the procedure of Curran et al. 2010), and the (R–K) colour: (1) Bianchi et al. (2014); (2) Abazajian et al. (2009); (2) Monet & et al. (2003); (4) Cutri et al. (2003); (5) Massaro et al. (2004); (6) Cutri et al. (2013); (7) Chen et al. (2005); (8) Howard et al. (2004); (9) Odell et al. (1978); (10) Raiteri et al. (2009); (11) Urry et al. (2000); (12) Zacharias et al. (2004); (13) Véron-Cetty & Véron (2010); (14) Souchay et al. (2015); (15) Healey et al. (2008); (16) Rao et al. (2006); (17) Fedorov et al. (2011); (18) Kuhn (2004).

The above redshift dependence of the strength of associated HI 21-cm absorption could stem from a variety of reasons: (1) less neutral hydrogen in high- z AGN environments, implying lower HI column densities, (2) higher gas spin temperatures in high- z environments, as has been seen in “intervening” galaxies towards AGNs, the damped Lyman- α absorbers (e.g. Kanekar & Chengalur 2003; Kanekar et al.

2014), or (3) lower covering factors in the high- z AGN sample, yielding a lower *observed* HI 21-cm optical depth. Unfortunately, in the case of associated HI 21-cm studies, we do not have direct estimates of the HI column density, and hence cannot separate between the first two possibilities, a low HI column density or a high gas spin temperature. We will initially consider the low covering factor hypothesis to

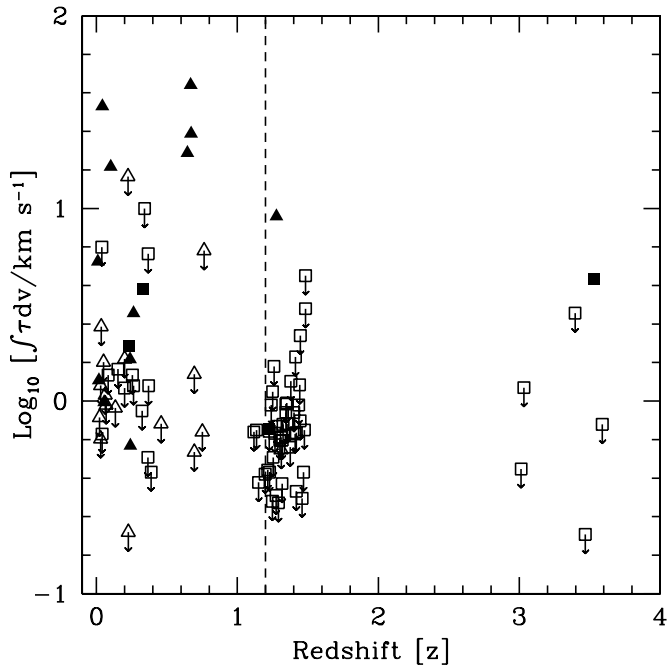


Figure 2. The velocity-integrated HI 21-cm optical depth of the 92 CJF sources of the sample, plotted as a function of redshift. The 63 sources observed in the present GMRT survey are shown by squares, while the 29 sources from the literature are represented by triangles. Filled symbols indicate detections of HI 21-cm absorption, while open symbols indicate upper limits on the HI 21-cm optical depth. The dashed vertical line indicates the median redshift of the sample, $z_{\text{med}} = 1.2$.

account for the low detection rate of HI 21-cm absorption, before investigating whether AGN conditions might yield either a low gas content or a high spin temperature.

5.3 Covering factor issues: The radio spectral index

A possible cause for the lower strength of associated HI 21-cm absorption in high- z AGNs is that the gas covering factor is systematically lower in the high-redshift systems. In such a scenario, the observed difference between the HI 21-cm absorption properties of the low- z and high- z sub-samples would arise not due to changes in the properties (e.g. HI column density or spin temperature) of neutral hydrogen in AGN environments, but due to differences in the structure of the radio emission in the high- z and low- z AGNs of the sample. Specifically, if the low-frequency radio emission of high- z AGNs arises primarily from extended structure (albeit still unresolved on GMRT baselines), which is not occulted by foreground gas clouds, the HI 21-cm optical depth estimated via the GMRT observations could be significantly lower than the true optical depth. For example, the radio emission of the low- z AGNs at the redshifted HI 21-cm line frequency might predominantly arise from a compact radio core, while that of the high- z AGNs might arise from either the radio jet or radio lobes.

The simplest way of testing the above scenario is to measure the fraction of radio emission arising from the AGN

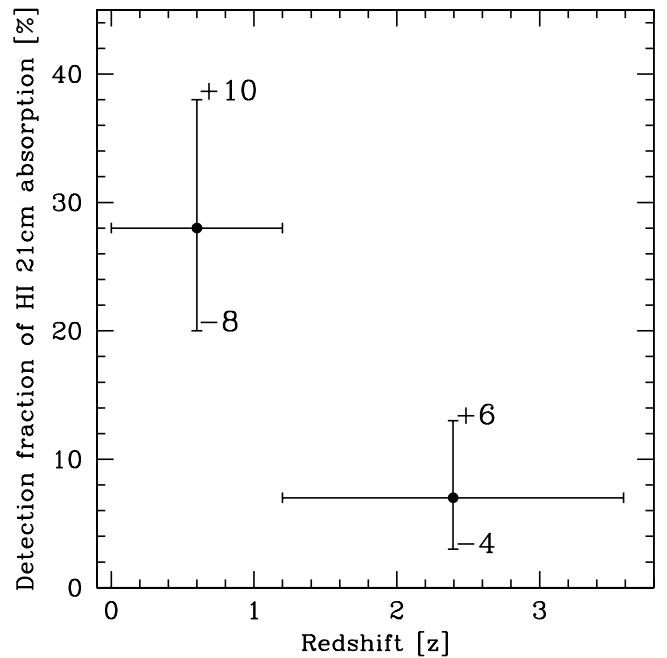


Figure 3. The detection rate of HI 21-cm absorption for the low- z and high- z sub-samples, separated at the median redshift.

core at, or close to, the redshifted HI 21-cm line frequency, via high-resolution VLBI imaging studies (e.g. Kanekar et al. 2009, 2014). This core fraction then gives a lower limit to the covering factor, under the assumption that the foreground gas clouds are likely to cover the core. Unfortunately, VLBI observations at frequencies $\lesssim 1$ GHz are technically challenging and are hence not available for most of the AGNs of our sample.

An alternative approach to addressing the covering factor issue is based on the fact that the compact emission from the core tends to undergo synchrotron self-absorption and hence typically has an inverted or flat spectrum, while extended radio emission from the radio jet or the lobes tends to have a steep spectrum. If the radio emission of the high- z AGNs at the redshifted HI 21-cm line frequency is dominated by the extended structure, yielding a low covering factor, one would expect these AGNs to have a systematically steeper spectral index at the HI 21-cm line frequency than the AGNs of the low- z sub-sample. We note that, although our target AGNs have been uniformly chosen from the CJF sample, with flat spectral indices, $\alpha \geq -0.5$ (Taylor et al. 1996), the CJF spectral index criterion is based on the AGN flux densities at two relatively high frequencies, 1.4 GHz and 4.85 GHz. It is hence possible that the radio emission at the low redshifted HI 21-cm line frequency is dominated by steep-spectrum extended structure, rather than by the flat- or inverted-spectrum radio core.

We will hence use the AGN's radio spectral index $\alpha_{21\text{-cm}}$ at the redshifted HI 21-cm frequency as a proxy for the compactness of the AGN. A flat or an inverted spectrum near the redshifted HI 21-cm line frequency ($\alpha_{21\text{-cm}} \gtrsim 0$) would indicate a core-dominated source, and a relatively high covering factor ($f \approx 1$), whereas a steep spectrum ($\alpha_{21\text{-cm}} \lesssim -0.7$)

would indicate extended radio structure and a possibly low covering factor ($f \ll 1$). If the measured HI 21-cm optical depths are found to depend on the spectral index, or if the high- z AGN sub-sample has a systematically steeper spectral index than the low- z sample, it would suggest that a low covering factor may be the cause of the lower observed HI 21-cm optical depths at high redshifts.

Figure 4[A] shows the integrated HI 21-cm optical depths of the 92 CJF sources of our sample plotted against $\alpha_{21\text{-cm}}$. While there are clearly a few sources with $\alpha_{21\text{-cm}} \lesssim -0.5$, most of the AGNs are seen to have flat radio spectra, $\alpha_{21\text{-cm}} \approx 0$. Indeed, the median spectral index of the sample, $\alpha_{21\text{-cm,med}} = -0.015$, is very close to zero, indicating that the sample is dominated by compact objects, with $\alpha_{21\text{-cm}} > -0.5$. A Peto-Prentice two-sample test finds that the distributions of the HI 21-cm optical depths of the two sub-samples, separated at the median $\alpha_{21\text{-cm}}$, are consistent (within $\approx 1.3\sigma$ significance) with the null hypothesis of being drawn from the same underlying distribution. We thus find no evidence for a dependence of the strength of the associated HI 21-cm absorption on the AGN spectral index.

Figure 4[B] shows the low-frequency AGN spectral index $\alpha_{21\text{-cm}}$ plotted against redshift; no trend is apparent in the figure. A Gehan-Wilcoxon two-sample test comparing the distributions of $\alpha_{21\text{-cm}}$ values of the low- z and the high- z sub-samples, separated at $z_{\text{med}} = 1.2$, finds that the data are consistent (within $\approx 1.2\sigma$ significance) with the null hypothesis of being drawn from the same underlying distribution. We thus find no evidence for a systematic difference between the spectral indices of the AGNs of the high- z and the low- z sub-samples.

In summary, we find no statistically significant evidence either that the strength of the HI 21-cm absorption depends on the low-frequency AGN spectral index or that the low-frequency spectral index varies systematically with redshift. Both of these would have been expected if low covering factors are the cause of the weaker HI 21-cm absorption observed in the high- z AGN sub-sample. We hence conclude that it is unlikely that the observed differences in the HI 21-cm absorption properties of the low- z and high- z AGN sub-samples can be explained by covering factor issues.

5.4 The AGN colour: Evidence for dust reddening?

For red quasars, the high extinction at optical wavebands is believed to be caused by dust extinction (e.g. Webster et al. 1995). However, it has also been suggested in the literature that not all red quasars are dusty systems (e.g. Benn et al. 1998). Earlier HI 21-cm studies have yielded ambiguous results: for example, Carilli et al. (1998b) detected strong HI 21-cm absorption in four out of five red quasars at intermediate redshifts ($z \approx 0.7$), suggesting a high HI column consistent with the dust obscuration hypothesis. Strong molecular absorption has also only been seen in very red AGNs (e.g. Wiklind & Combes 1994; Wiklind & Combes 1996; Kanekar & Chengalur 2002; Kanekar et al. 2005). However, later HI 21-cm absorption studies have found no significant correlation between the detectability of associated HI 21-cm absorption and the AGN colour (e.g. Curran et al. 2008; Aditya et al. 2016), suggesting that the reddening may have other causes besides dust obscuration. Our detection of

associated HI 21-cm absorption towards TXS 1456+375 is consistent with the dust-reddening hypothesis.

It has long been known that the Galactic extinction at 5500 Å is proportional to the total hydrogen column density, with $A_V = 6.29 \times 10^{-22} [N_{\text{HI}} + 2N_{\text{H}_2}]$ (e.g. Savage et al. 1977). This is understood as arising due to reddening produced by the large amounts of dust associated with a high hydrogen column. Webster et al. (1995) hence suggested that “red” quasars, with a steeper spectral index between the optical and NIR wavebands than typical quasars, are likely to acquire their redder colours due to dust extinction. Consistent with this hypothesis, Carilli et al. (1998b) found that 80% of red quasars showed either associated or intervening HI 21-cm absorption, while only 11% of optically-selected MgII absorbers showed radio absorption. Similarly, all five of the known redshifted radio molecular absorbers at $z > 0.2$ have background quasars with extremely red colours, $(R-K) > 4$ (Wiklind & Combes 1994; Wiklind & Combes 1995, 1996, 1997; Kanekar & Chengalur 2002; Kanekar et al. 2005; Curran et al. 2006, 2008). Our detection of associated HI 21-cm absorption towards TXS 1456+375 is consistent with the dust-reddening hypothesis.

However, it has also been noted in the literature that not all red quasars appear to be dusty systems (e.g. Benn et al. 1998). Indeed, recent searches for associated HI 21-cm absorption in red AGNs have not been very successful (e.g. Yan et al. 2016), while no significant correlation has been found between the detectability of associated HI 21-cm absorption and the AGN colour (e.g. Curran et al. 2008; Aditya et al. 2016), suggesting that the reddening may have other causes besides dust obscuration. We note that the sample of Carilli et al. (1998b) was very small (five systems), and limited to low redshifts, $z \lesssim 0.7$.

In this section, we test the hypothesis that associated HI 21-cm absorption is more likely to arise in red AGNs, by examining our sample for a correlation between the strength of the HI 21-cm absorption with AGN (R-K) colour. Unfortunately, NIR photometry was available for 58 AGNs of the sample and so the present analysis is restricted to these 58 systems.

At the outset, we note that the choice of a flat-spectrum sample is likely to be biased against the reddest sightlines. In standard unification schemes (e.g. Urry & Padovani 1995), a flat AGN spectrum is expected to mostly arise from sightlines closer to orthogonal to the obscuring torus. Such sightlines are unlikely to be affected by extinction from dust in the torus, and so we do not expect very large (R-K) values, $(R-K) \gtrsim 5$, in our sample.

Fig. 5 shows the integrated HI 21-cm optical depth plotted versus the (R-K) colour for the 58 AGNs with NIR photometry. Of the 12 AGNs with detections of HI 21-cm absorption, five have relatively red colours, $(R-K) > 3$. Further, three of these five systems lie at the top right of the figure, indicating both red colours and high integrated HI 21-cm optical depths; indeed, these three AGNs have $(R-K) > 5$, comparable to the colours of the AGNs that show molecular absorption! At least for these systems, the red colours are likely to arise due to the presence of high columns of gas and associated dust at the AGN redshift. However, we also note that there are four AGNs that show HI 21-cm absorption at relatively low (R-K) values, $(R-K) \lesssim 1.3$, and that one

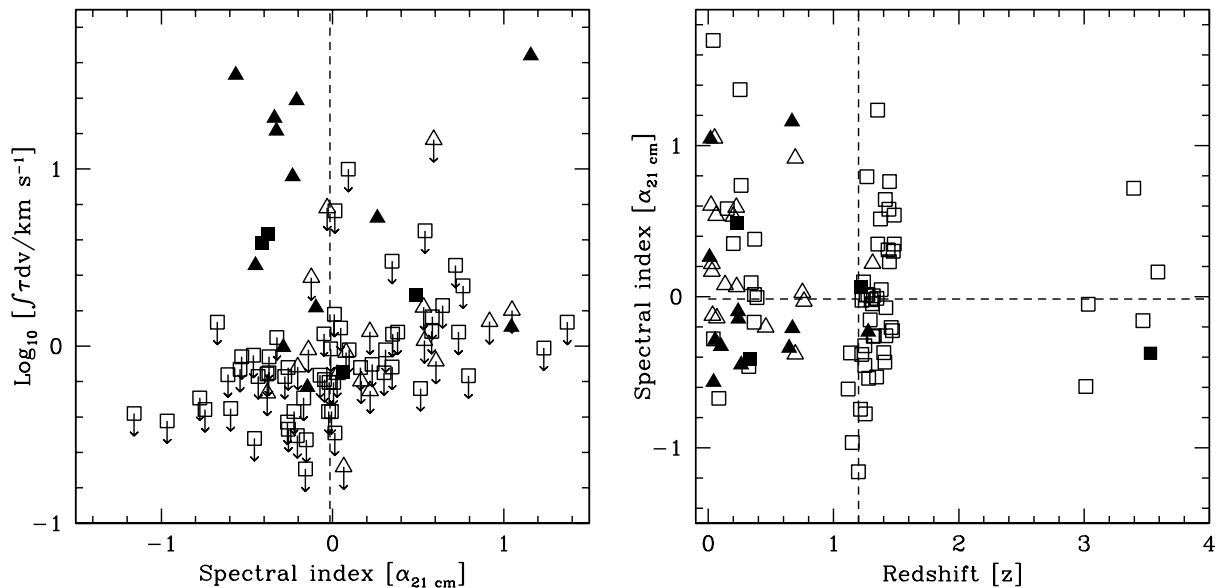


Figure 4. [A] Left panel: The integrated HI 21-cm optical depth of the 92 CJF sources plotted against the spectral index, $\alpha_{21\text{-cm}}$, around the redshifted HI 21-cm line frequency; the dashed vertical line indicates the median spectral index, $\alpha_{21\text{-cm,med}} = -0.015$. [B] Right panel: The spectral index $\alpha_{21\text{-cm}}$, plotted against AGN redshift; the dashed vertical line indicates the median redshift, $z_{\text{med}} = 1.2$, while the dashed horizontal line indicates the median spectral index, $\alpha_{21\text{-cm}} = -0.015$. In both panels, the 63 AGNs of our survey are shown as squares, while the 29 literature sources are shown as triangles. Filled symbols represent detections, while open symbols represent upper limits on the integrated HI 21-cm optical depth. See main text for discussion.

of these has the second-highest integrated HI 21-cm optical depth of the full sample.

To test the dependence of the strength of the HI 21-cm absorption on the (R–K) colour, we divided the sample of 58 systems at the median (R–K) value, $(R-K) = 2.38$, and carried out two-sample tests on the high-(R–K) and low-(R–K) sub-samples. A Peto-Prentice two-sample test for censored data finds that the null hypothesis that the sub-samples are drawn from the same underlying distribution is rejected at only 1.4σ significance. The two sub-samples are thus consistent with being drawn from the same distribution, and we find no statistically significant evidence for a dependence of the strength of HI 21-cm absorption on the (R–K) colour of the AGN. Thus, while three of the four highest integrated HI 21-cm optical depths do arise from the reddest AGNs, our results from the CJF sample do not provide support for the dust-reddening hypothesis.

5.5 Effects of the AGN luminosity

As mentioned briefly in Section 5.1, a high AGN luminosity can adversely affect the strength of the associated HI 21-cm absorption (e.g. Curran et al. 2008, 2013). This is because a high UV luminosity can cause ionization of the nearby neutral hydrogen, thus reducing the HI column density, and can also affect the spin temperature (which is coupled to the colour temperature of the Lyman- α radiation field; Wouthuysen 1952; Field 1958; Field 1959). Similarly, a high AGN rest-frame 1.4 GHz luminosity can raise the gas spin temperature (Field 1958; Field 1959). Both a decrease in the HI column density and a raising of the spin temperature would reduce the strength of the HI 21-cm absorption. Thus, if the higher-redshift AGNs of our sample tend to have

higher UV and/or radio luminosities, this would provide an alternative explanation of the weaker HI 21-cm absorption in the high- z sub-sample.

Figs. 6[A] and [B] show, respectively, the rest-frame UV 1216 Å luminosity and the rest-frame 1.4 GHz radio luminosity of the sources of the CJF sample plotted against redshift. In both panels, the vertical dashed line is at the median redshift of the sample, while the horizontal dashed line is at the median luminosity. It is clear that the high- z AGNs of the sample typically lie close to or above the median luminosity (in both UV and radio wavebands), while the low- z AGNs mostly lie below the median luminosity. Again dividing the sample at $z_{\text{med}} = 1.2$, a Gehan-Wilcoxon test finds that the null hypothesis that the rest-frame UV and radio luminosities of the two sub-samples are drawn from the same distribution is rejected, respectively, at $\approx 7.7\sigma$ and $\approx 7.8\sigma$ significance. As such, it is clear that the sample contains a strong bias towards higher UV and radio luminosities at high redshifts. We note, in passing, that the rest-frame UV 1216 Å and radio 1.4 GHz luminosities of the sources in our sample are strongly correlated (at $\approx 9\sigma$ significance, via a Kendall-tau test).

It thus appears that the apparent redshift evolution in the strength of the associated HI 21-cm absorption might also arise due to differences in the UV and/or radio luminosities of the AGNs of the low- z and the high- z sub-samples. Figs. 7[A] and [B] plot the integrated HI 21-cm optical depth versus, respectively, the rest-frame UV 1216 Å luminosity and the rest-frame radio 1.4 GHz luminosity (with all quantities in logarithmic units). The dashed vertical lines in the two figures indicate the median luminosities, $L_{\text{UV,med}} = 10^{22.64} \text{ W Hz}^{-1}$ and $L_{1.4\text{GHz,med}} = 10^{27.17} \text{ W Hz}^{-1}$, respectively. It is clear that most of the detections of HI 21-cm

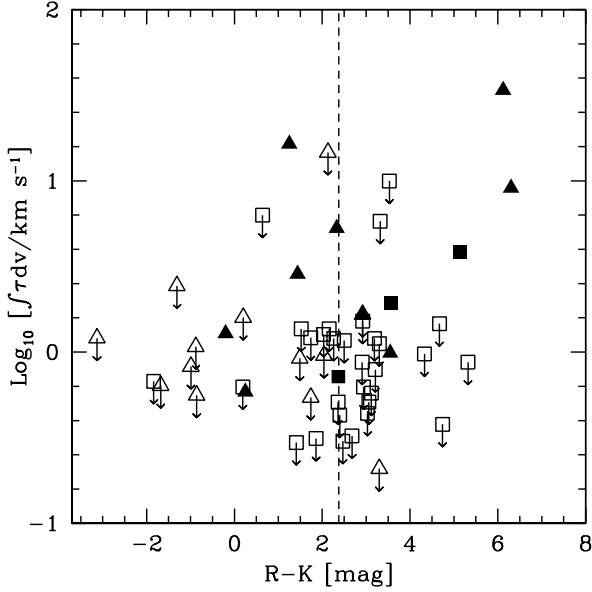


Figure 5. The integrated HI 21-cm optical depth, in logarithmic units, plotted against the (R-K) colour for the 58 AGNs of the sample with NIR photometry. The dashed vertical line indicates the median colour, (R-K) = 2.38. The sources from our survey and the literature are shown as squares and triangles, respectively. Detections of HI 21-cm absorption are shown as filled symbols and non-detections as open symbols. See main text for discussion.

absorption lie in the low-luminosity halves of the two figures; further, the integrated HI 21-cm optical depths towards low-luminosity AGNs appear higher than the typical 3σ upper limits on the integrated HI 21-cm optical depths towards AGNs with high luminosities. Formally, a Peto-Prentice two-sample test (for censored data) finds that the null hypothesis that the HI 21-cm optical depth distributions of the low-luminosity and high-luminosity sub-samples are drawn from the same distribution is rejected at, respectively, $\approx 3.6\sigma$ and $\approx 3.3\sigma$ significance, for the rest-frame UV 1216 Å and rest-frame radio 1.4 GHz luminosities.

We thus find statistically significant evidence for a dependence of the strength of associated HI 21-cm absorption in the CJF sample on both redshift and AGN luminosity in the rest-frame UV 1216 Å and radio 1.4 GHz wavebands, but not on the low-frequency radio spectral index or the (R-K) colour. Weaker HI 21-cm absorption is obtained at higher redshifts and higher radio and UV luminosities. Unfortunately, there is a strong correlation between AGN luminosity and redshift in the AGNs of our sample (see Figs. 6[A] and [B]), due to which it is not currently possible to break the degeneracy between redshift and luminosity, and identify the primary cause, if any, for the differences in the strength of the HI 21-cm absorption. Searches for HI 21-cm absorption in either a low-luminosity AGN sample at high redshifts, or a high-luminosity sample at low redshifts would be required to break the present degeneracy.

6 SUMMARY

We have used the GMRT to carry out a search for associated HI 21-cm absorption in 50 flat-spectrum AGNs, selected from the CJF sample. The data on ten AGNs were rendered unusable by RFI. We obtained new detections of HI 21-cm absorption in two sources, at $z = 0.229$ towards TXS 0003+380 and $z = 0.333$ towards TXS 1456+375, and also confirmed an earlier detection (by Curran et al. 2013) of HI 21-cm absorption at $z = 1.277$ towards TXS 1543+480. The measured velocity-integrated HI 21-cm optical depths towards the above three AGNs lie in the range $\int \tau dv \approx 1.9\text{--}9.6 \text{ km s}^{-1}$, implying HI column densities of $\approx (3.5\text{--}17.5) \times 10^{20} \text{ cm}^{-2}$, for an assumed spin temperature of 100 K and covering factor of unity. For the remaining 37 AGNs, the 3σ upper limits on the integrated HI 21-cm optical depth range from 0.3 – 14 km s^{-1} , with a median value of $\approx 0.97 \text{ km s}^{-1}$.

Our full sample of CJF sources with searches for redshifted HI 21-cm absorption consists of 92 AGNs, 63 from our survey (including 24 sources from Aditya et al. 2016, 2017) and 29 from the literature. This is currently the largest sample of uniformly-selected AGNs with searches for associated HI 21-cm absorption, with 16 HI 21-cm detections and 76 non-detections, at redshifts 0.01 – 3.6, and with a median redshift of $z_{\text{med}} = 1.2$.

We find that both the strength and the detectability of HI 21-cm absorption appear higher at low redshifts, $z < z_{\text{med}}$. The detection rate of HI 21-cm absorption is $28_{-8}^{+10}\%$ for the low- z AGN sub-sample (with $z < 1.2$), but only $7_{-4}^{+6}\%$ for the high- z sub-sample (with $z > 1.2$). While the difference in detection rates has only $\approx 2.1\sigma$ significance, a Peto-Prentice two-sample test on the velocity integrated HI 21-cm optical depths finds that the null hypothesis that the low- z and high- z sub-samples are drawn from the same distribution is ruled out at $\approx 3\sigma$ significance. We thus obtain statistically-significant evidence for redshift evolution in the strength of associated HI 21-cm absorption in the Caltech-Jodrell Flat-spectrum AGN sample.

However, we also found evidence for a significant bias in the intrinsic luminosities of the AGNs of our sample, with the high- z AGNs having higher rest-frame 1216 Å UV and 1.4 GHz radio luminosities. Examining the dependence of the strength of the HI 21-cm absorption on AGN luminosity, the null hypothesis that the velocity-integrated HI 21-cm optical depths of the high-luminosity and low-luminosity AGNs arise from the same distribution is ruled out at $\approx (3.3\text{--}3.6)\sigma$ significance in a Peto-Prentice two-sample test (for the 1216 Å UV and 1.4 GHz radio luminosities).

We also examined the possibility that the lower strength of HI 21-cm absorption in high- z AGNs might arise due to a typically lower covering factor for the high- z sub-sample. This could occur if the radio continuum at the redshifted HI 21-cm line frequency for the high- z sub-sample is dominated by extended emission. We used the AGN spectral index around the redshifted HI 21-cm line frequency as a proxy for source compactness, since extended emission is expected to have a steep spectrum. We find no evidence in two-sample tests that the strength of the HI 21-cm absorption depends on AGN spectral index, or that the spectral index itself depends on the AGN redshift. It is hence unlikely that the ob-

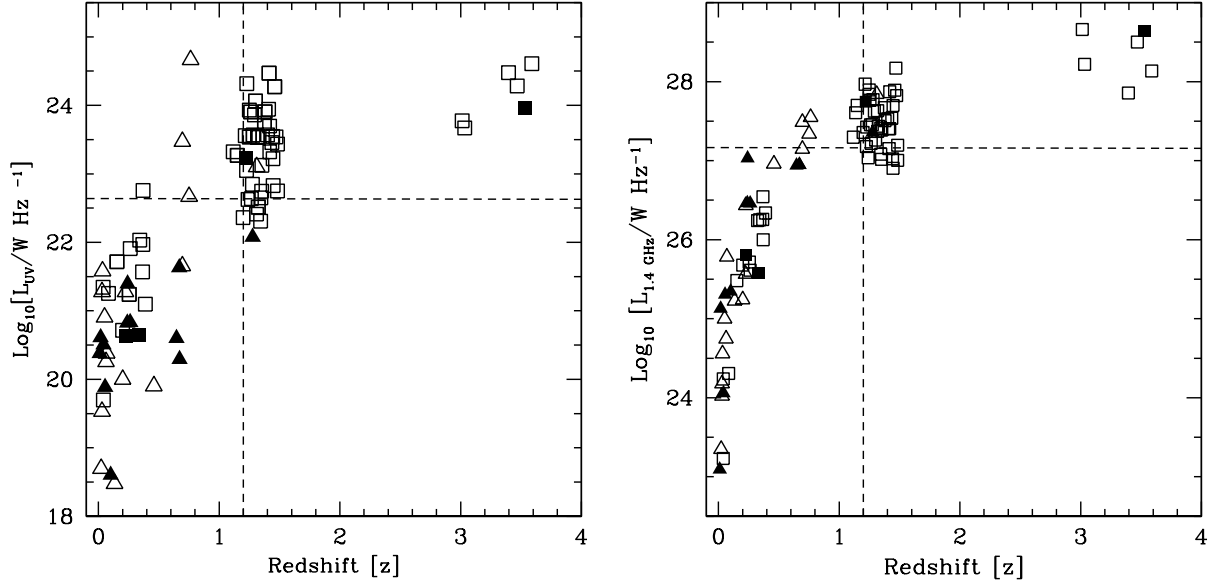


Figure 6. The AGN luminosities of the CJF sources of the sample in [A] (left panel) at rest-frame UV 1216 Å (87 sources) and [B] (right panel) rest-frame radio 1.4 GHz (92 sources), plotted, in logarithmic units, against the AGN redshift. The dashed vertical lines indicate the median redshift, z_{med} , while the dashed horizontal lines indicate the median UV 1216 Å and radio 1.4 GHz luminosities ($L_{UV,med} = 10^{22.64} \text{ W Hz}^{-1}$ and $L_{1.4 \text{ GHz},med} = 10^{27.17} \text{ W Hz}^{-1}$, respectively). The squares and triangles represent, respectively, the sources from our survey and the literature. Filled and open symbols represent, respectively, HI 21-cm detections and upper limits on the integrated HI 21-cm optical depth. See text for discussion.

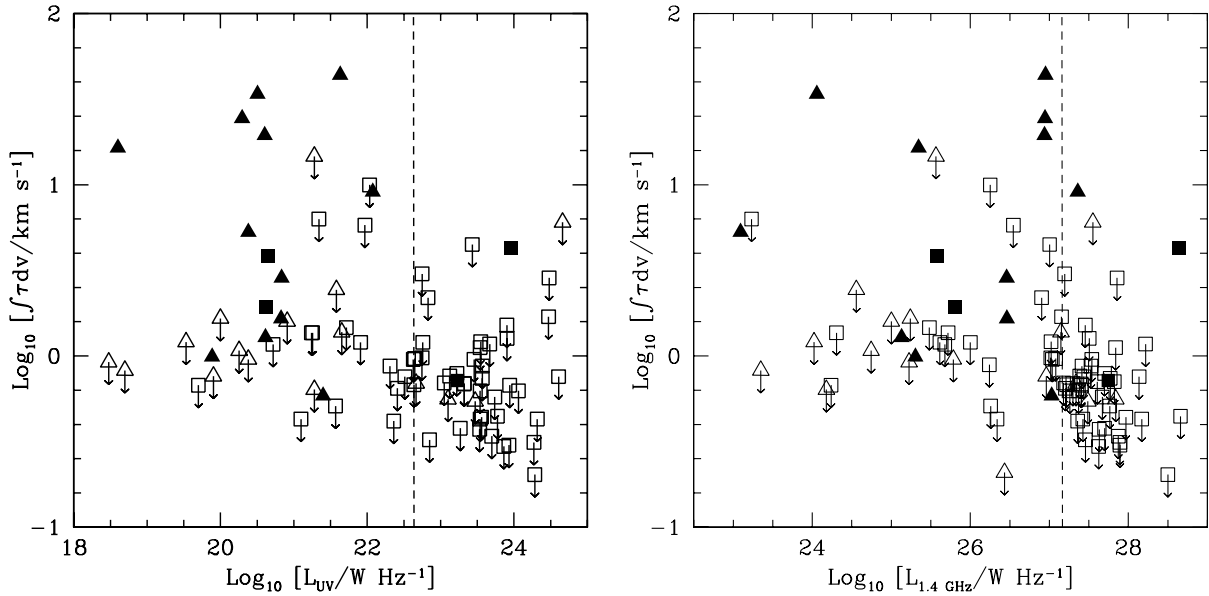


Figure 7. The integrated HI 21-cm optical depths of the AGNs of the our sample plotted against [A] (left panel) the rest-frame UV 1216 Å luminosity and [B] (right panel) the rest-frame radio 1.4 GHz luminosity, with all quantities in logarithmic units. The dashed vertical lines indicate the median UV 1216 Å and radio 1.4 GHz luminosities ($L_{UV,med} = 10^{22.64} \text{ W Hz}^{-1}$ and $L_{1.4 \text{ GHz},med} = 10^{27.17} \text{ W Hz}^{-1}$, respectively). The sources from our survey and the literature are represented by squares and triangles, respectively. Filled and open symbols represent, respectively, detections and upper limits on the HI 21-cm optical depth.

served weakness of the HI 21-cm absorption in high- z AGNs arises due to a low covering factor.

We find no statistically-significant evidence that the strength of HI 21-cm absorption depends on AGN colour. However, five of the 12 AGNs with HI 21-cm detections and

estimates of the (R-K) colour show relatively red colours, with $(R-K) > 3$. Three of these systems have both high integrated HI 21-cm optical depths and $(R-K) > 5$; for these, the red colour is likely to arise due to dust at the AGN redshift.

The above results are consistent with those from our

pilot GMRT HI 21-cm absorption survey of the CJF sample Aditya et al. (2016), but are now based on a significantly larger AGN sample (92 AGNs against 52 in Aditya et al. 2016), and with more than half the sample at $z > 1$. The median redshift of the present sample ($z_{\text{med}} = 1.2$) is also significantly higher than that ($z_{\text{med}} = 0.76$) of Aditya et al. (2016).

In summary, the strength of associated HI 21-cm absorption in the CJF AGN sample appears to depend on both redshift and AGN luminosity, with weaker HI 21-cm absorption at high redshifts and high luminosities. This could arise due to (1) lower amounts of neutral gas in high- z , high-luminosity AGN environments, due to either redshift evolution or ionization of the HI by the far-UV AGN radiation, or (2) higher spin temperatures in high- z , high-luminosity AGN environments, due to either a preponderance of warm neutral gas around high- z AGNs or spin temperatures greater than the kinetic temperature due to the high AGN UV/radio luminosity. Unfortunately, the luminosity bias in our sample, with the higher-luminosity AGNs located at higher redshifts, implies that the present dataset does not allow us to distinguish between the above possibilities to identify whether redshift or AGN luminosity is the primary driving factor in determining the strength of the associated HI 21-cm absorption; this will be the focus of future studies.

ACKNOWLEDGEMENTS

We thank the staff of the GMRT who have made these observations possible. The GMRT is run by the National Centre for Radio Astrophysics of the Tata Institute of Fundamental Research. NK acknowledges support from the Department of Science and Technology via a Swarnajayanti Fellowship (DST/SJF/PSA-01/2012-13). JA was supported during a part of this work by the Indo-French Centre for the Promotion of Advanced Research under Project 5504-B (PIs: N. Gupta, P. Noterdaeme).

REFERENCES

- Abazajian K. N., et al., 2009, *ApJS*, 182, 543
 Aditya J. N. H. S., Kanekar N., 2018, *MNRAS*, 473, 59
 Aditya J. N. H. S., Kanekar N., Kurapati S., 2016, *MNRAS*, 455, 4000
 Aditya J. N. H. S., Kanekar N., Prochaska J. X., Day B., Lynam P., Cruz J., 2017, *MNRAS*, 465, 5011
 Allison J. R., et al., 2012, *MNRAS*, 423, 2601
 Becker R. H., White R. L., Helfand D. J., 1995, *ApJ*, 450, 559
 Benn C. R., Vigotti M., Carballo R., Gonzalez-Serrano J. I., Sánchez S. F., 1998, *MNRAS*, 295, 451
 Beswick R. J., Pedlar A., Holloway A. J., 2002, *MNRAS*, 329, 620
 Bianchi L., Conti A., Shiao B., 2014, *Advances in Space Research*, 53, 900
 Carilli C. L., Wrobel J. M., Ulvestad J. S., 1998a, *AJ*, 115, 928
 Carilli C. L., Menten K. M., Reid M. J., Rupen M. P., Yun M. S., 1998b, *ApJ*, 494, 175
 Chandola Y., Sirothia S. K., Saikia D. J., 2011, *MNRAS*, 418, 1787
 Chandola Y., Gupta N., Saikia D. J., 2013, *MNRAS*, 429, 2380
 Chen P. S., Fu H. W., Gao Y. F., 2005, *New Astron.*, 11, 27
 Condon J. J., Cotton W. D., Greisen E. W., Yin Q. F., Perley R. A., Taylor G. B., Broderick J. J., 1998, *AJ*, 115, 1693
 Conway J. E., 1999, in Carilli C. L., Radford S. J. E., Menten K. M., Langston G. L., eds, *Astronomical Society of the Pacific Conference Series Vol. 156, Highly Redshifted Radio Lines*. p. 259
 Curran S. J., Whiting M. T., Murphy M. T., Webb J. K., Longmore S. N., Pihlström Y. M., Athreya R., Blake C., 2006, *MNRAS*, 371, 431
 Curran S. J., Whiting M. T., Wiklind T., Webb J. K., Murphy M. T., Purcell C. R., 2008, *MNRAS*, 391, 765
 Curran S. J., Tzanavaris P., Darling J. K., Whiting M. T., Webb J. K., Bignell C., Athreya R., Murphy M. T., 2010, *MNRAS*, 402, 35
 Curran S. J., Whiting M. T., Sadler E. M., Bignell C., 2013, *MNRAS*, 428, 2053
 Cutri R. M., et al., 2003, *2MASS All Sky Catalog of point sources*.
 Cutri R. M., et al., 2013, *Technical report, Explanatory Supplement to the ALLWISE Data Release Products*
 Davenport J. R. A., Ruan J. J., Becker A. C., Macleod C. L., Cutri R. M., 2015, *ApJ*, 803, 2
 De Young D. S., Roberts M. S., Saslaw W. C., 1973, *ApJ*, 185, 809
 Dickey J. M., 1986, *ApJ*, 300, 190
 Dickey J. M., Benson J. M., 1982, *AJ*, 87, 278
 Douglas J. N., Bash F. N., Bozyan F. A., Torrence G. W., Wolfe C., 1996, *AJ*, 111, 1945
 Dwarakanath K. S., Owen F. N., van Gorkom J. H., 1995, *ApJ*, 442, L1
 Fanaroff B. L., Riley J. M., 1974, *MNRAS*, 167, 31
 Fedorov P. N., Akhmetov V. S., Bobylev V. V., 2011, *MNRAS*, 416, 403
 Fey A. L., Charlot P., 2000, *ApJS*, 128, 17
 Field G. B., 1958, *Proc. I. R. E.*, 46, 240
 Field G. B., 1959, *ApJ*, 129, 536
 Gallimore J. F., Baum S. A., O’Dea C. P., Pedlar A., Brinks E., 1999, *ApJ*, 524, 684
 Gardner F. F., Whiteoak J. B., 1976, *MNRAS*, 175, 9
 Gehrels N., 1986, *ApJ*, 303, 336
 Geréb K., Maccagni F. M., Morganti R., Oosterloo T. A., 2015, *A&A*, 575, 44
 Ghisellini G., Padovani P., Celotti A., Maraschi L., 1993, *ApJ*, 407, 65
 Glikman E., et al., 2012, *ApJ*, 757, 51
 Greisen E. W., 2003, in Heck A., ed., *Astrophysics and Space Science Library Vol. 285, Information Handling in Astronomy - Historical Vistas*. p. 109
 Gupta N., Salter C. J., Saikia D. J., Ghosh T., Jeyakumar S., 2006, *MNRAS*, 373, 972
 Healey S. E., et al., 2008, *ApJS*, 175, 97
 Heeschen D. S., 1984, *AJ*, 89, 1111
 Helmboldt J. F., et al., 2007, *ApJ*, 658, 203
 Henstock D. R., Browne I. W. A., Wilkinson P. N., Taylor G. B., Vermeulen R. C., Pearson T. J., Readhead A. C. S., 1995, *ApJS*, 100, 1
 Howard E. S., Webb J. R., Pollock J. T., Stencil R. E., 2004, *AJ*, 127, 17
 Isobe T., Feigelson E. D., Nelson P. I., 1986, *ApJ*, 306, 490
 Kanekar N., Chengalur J. N., 2002, *A&A*, 381, L73
 Kanekar N., Chengalur J. N., 2003, *A&A*, 399, 857
 Kanekar N., Chengalur J. N., 2008, *MNRAS*, 384, L6
 Kanekar N., et al., 2005, *Phys. Rev. Lett.*, 95, 261301
 Kanekar N., Lane W. M., Momjian E., Briggs F. H., Chengalur J. N., 2009, *MNRAS*, 394, L61
 Kanekar N., et al., 2014, *MNRAS*, 438, 2131
 Kellermann K. I., Pauliny-Toth I. I. K., 1981, *ARA&A*, 19, 373
 Kuhn O. P., 2004, *MNRAS*, 348, 647
 Labiano A., Vermeulen R. C., Barthel P. D., O’Dea C. P., Gallimore J. F., Baum S., de Vries W., 2006, *A&A*, 447, 481

- Maccagni F. M., Morganti R., Oosterloo T. A., Geréb K., Maddox N., 2017, *A&A*, 604, A43
- Mahony E. K., Morganti R., Emonts B. H. C., Oosterloo T. A., Tadhunter C., 2013, *MNRAS*, 435, L58
- Massaro E., Perri M., Giommi P., Nesci R., 2004, *A&A*, 413, 489
- Massaro E., Giommi P., Leto C., Marchegiani P., Maselli A., Perri M., Piranomonte S., Scavi S., 2009, *A&A*, 495, 691
- Monet D. G., et al. 2003, *AJ*, 125, 984
- Moore C. B., Carilli C. L., Menten K. M., 1999, *ApJ*, 510, L87
- Morganti R., Oosterloo T., 2018, *Astronomy & Astrophysics Review*, in press (arXiv:1807.01475)
- Morganti R., Oosterloo T. A., Tadhunter C. N., van Moorsel G., Killeen N., Wills K. A., 2001, *MNRAS*, 323, 331
- Morganti R., Oosterloo T. A., Emonts B. H. C., van der Hulst J. M., Tadhunter C. N., 2003, *ApJ*, 593, L69
- Morganti R., Oosterloo T. A., Tadhunter C. N., Vermeulen R., Pihlström Y. M., van Moorsel G., Wills K. A., 2004, *A&A*, 424, 119
- Morganti R., Tadhunter C. N., Oosterloo T. A., 2005, *A&A*, 444, L9
- Morganti R., Peck A. B., Oosterloo T. A., van Moorsel G., Capetti A., Fanti R., Parma P., de Ruiter H. R., 2009, *A&A*, 505, 559
- Morganti R., Fogasy J., Paragi Z., Oosterloo T., Orienti M., 2013, *Science*, 341, 1082
- Mundell C. G., Pedlar A., Baum S. A., O’Dea C. P., Gallimore J. F., Brinks E., 1995, *MNRAS*, 272, 355
- O’Dea C. P., 1998, *PASP*, 110, 493
- Odell S. L., Puschell J. J., Stein W. A., Owen F., Porcas R. W., Mufson S., Moffett T. J., Ulrich M.-H., 1978, *ApJ*, 224, 22
- Orienti M., Morganti R., Dallacasa D., 2006, *A&A*, 457, 531
- Owsianik I., Conway J. E., 1998, *A&A*, 337, 69
- Owsianik I., Conway J. E., Polatidis A. G., 1998, *A&A*, 336, L37
- Pearson T. J., Readhead A. C. S., 1988, *ApJ*, 328, 114
- Peck A. B., Taylor G. B., 1998, *ApJ*, 502, L23
- Peck A. B., Taylor G. B., Conway J. E., 1999, *ApJ*, 521, 103
- Pihlström Y. M., Conway J. E., Vermeulen R. C., 2003, *A&A*, 404, 871
- Raiteri C. M., et al., 2009, *A&A*, 507, 769
- Rao S. M., Turnshek D. A., Nestor D. B., 2006, *ApJ*, 636, 610
- Rengelink R. B., Tang Y., de Bruyn A. G., Miley G. K., Bremer M. N., Röttgering H. J. A., Bremer M. A. R., 1997, *A&AS*, 124, 259
- Roberts M. S., 1970, *ApJ*, 161, L9
- Savage B. D., Bohlin R. C., Drake J. F., Budich W., 1977, *ApJ*, 216, 291
- Schneider D. P., et al., 2005, *AJ*, 130, 367
- Shu F., 1991. University Science Books
- Souchay J., et al., 2015, *A&A*, 583, A75
- Stickel M., Kühr H., 1994, *A&AS*, 105, 67
- Struve C., Conway J. E., 2012, *A&A*, 546, 22
- Taylor G. B., Vermeulen R. C., Readhead A. C. S., Pearson T. J., Henstock D. R., Wilkinson P. N., 1996, *ApJS*, 107, 37
- Taylor G. B., Marr J. M., Pearson T. J., Readhead A. C. S., 2000, *ApJ*, 541, 112
- Urry C. M., Padovani P., 1995, *PASP*, 107, 803
- Urry C. M., Scarpa R., O’Dowd M., Falomo R., Pesce J. E., Treves A., 2000, *ApJ*, 532, 816
- Vermeulen R. C., et al., 2003, *A&A*, 404, 861
- Véron-Cetty M.-P., Véron P., 2010, *A&A*, 518, A10
- Webster R. L., Francis P. J., Petersont B. A., Drinkwater M. J., Masci F. J., 1995, *Nature*, 375, 469
- Wiklind T., Combes F., 1994, *A&A*, 286, L9
- Wiklind T., Combes F., 1995, *A&A*, 299, 382
- Wiklind T., Combes F., 1996, *A&A*, 315, 86
- Wiklind T., Combes F., 1997, *A&A*, 328, 48
- Wouthuysen S. A., 1952, *AJ*, 57, 31
- Yan T., Stocke J. T., Darling J., Momjian E., Sharma S., Kanekar N., 2016, *AJ*, 151, 74
- Zacharias N., Monet D. G., Levine S. E., Urban S. E., Gaume R., Wycoff G. L., 2004, in *American Astronomical Society Meeting Abstracts*. p. 1418
- van Gorkom J. H., Knapp G. R., Ekers R. D., Ekers D. D., Laing R. A., Polk K. S., 1989, *AJ*, 97, 708

APPENDIX A:

This paper has been typeset from a $\text{\TeX}/\text{\LaTeX}$ file prepared by the author.

Figure A1. The GMRT spectra for the 37 CJF sources with non-detections of HI 21-cm absorption. All spectra have been Hanning-smoothed and resampled. The shaded channels in the spectra are corrupted by RFI.

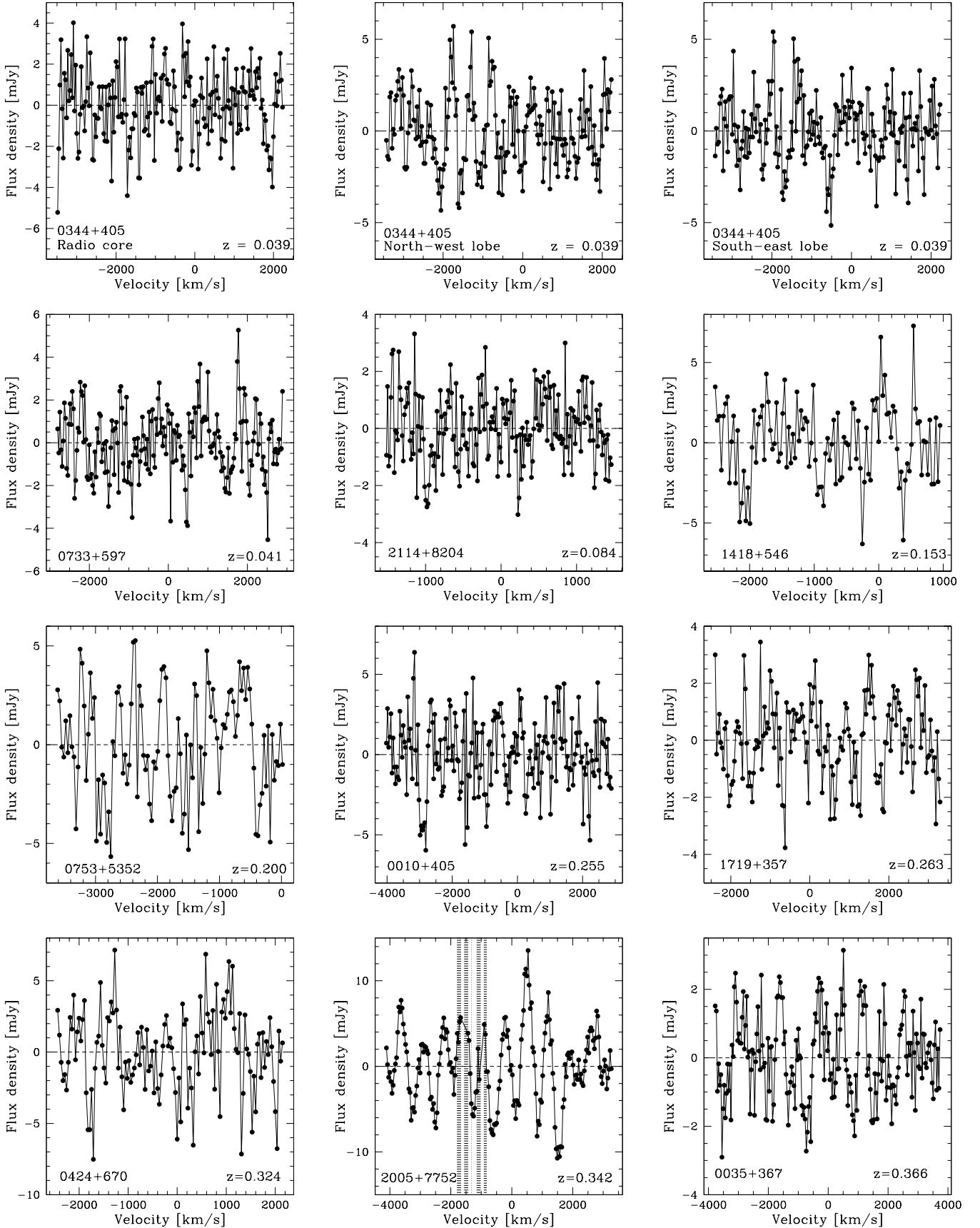


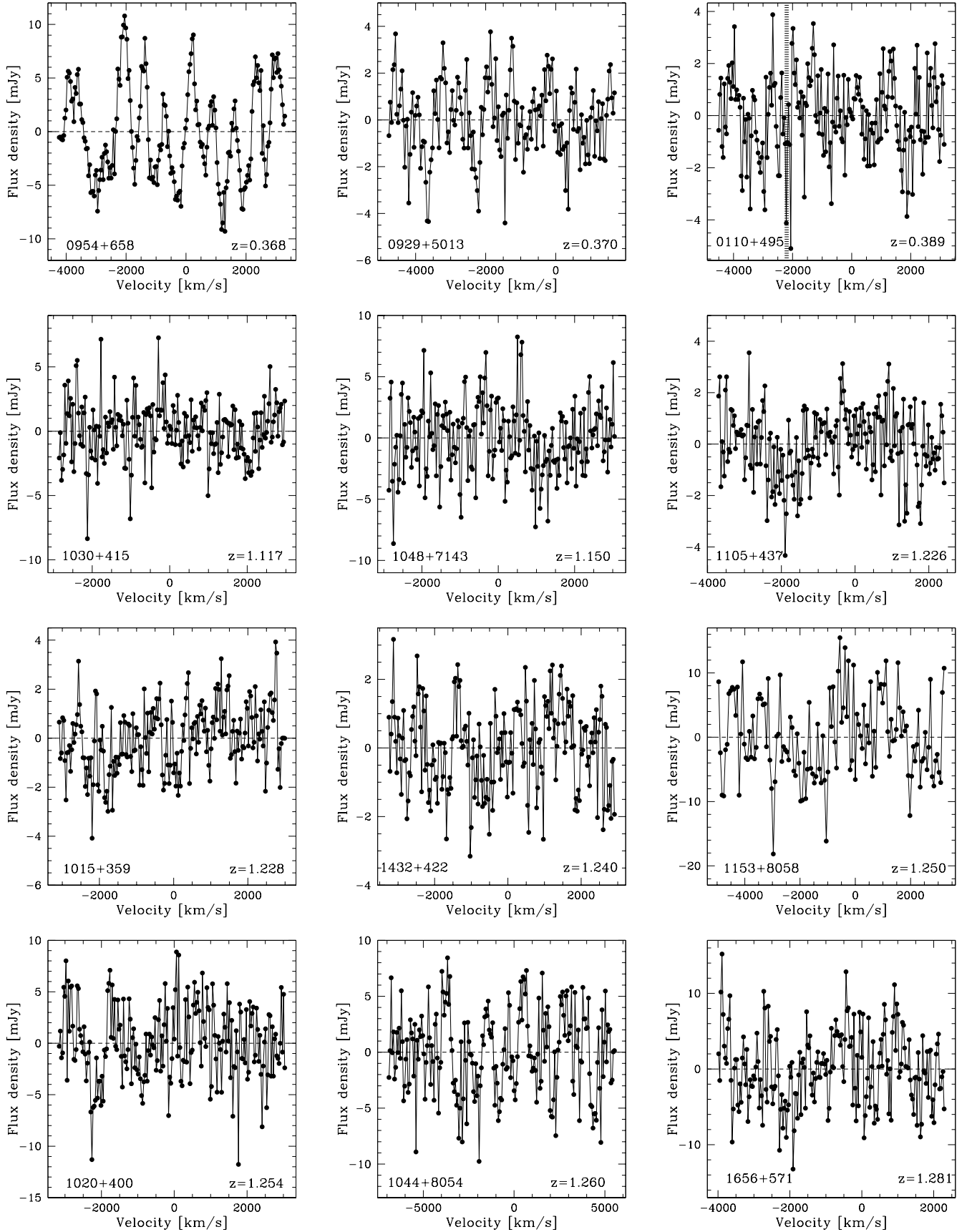
Figure A1. (contd.) The GMRT Hi 21-cm spectra for the 37 non-detections

Figure A1. (contd.) The GMRT HI 21-cm spectra for the 37 non-detections.

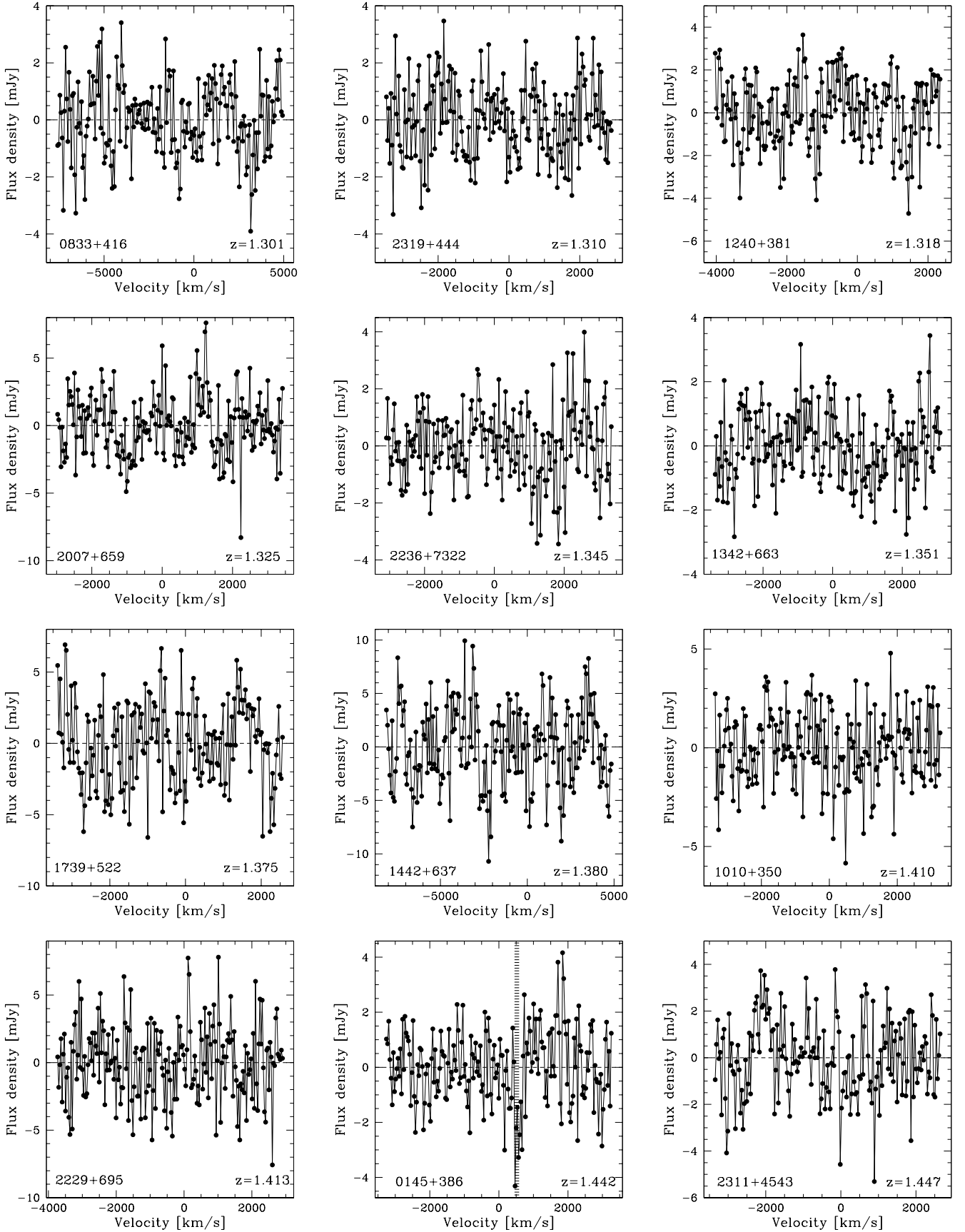


Figure A1. (contd.) The GMRT HI 21-cm spectra for the 37 non-detections.